Available online at www.sciencedirect.com
ScienceDirect
International Journal of Heat and Fluid Flow 28 (2007) 683–707
International Journal of HEAT AND FLUID FLOW
www.elsevier.com/locate/ijhff

Turbulent flow over transverse ribs in open channel with converging side walls

M.F. Tachie *, M. Agelinchaab, M.K. Shah

Department of Mechanical and Manufacturing Engineering, University of Manitoba, Winnipeg, Man., Canada R3T 5V6

Received 20 June 2006; received in revised form 4 August 2006; accepted 1 October 2006
Available online 27 November 2006

Abstract

This paper reports an experimental study of favorable pressure gradient turbulent flow over transverse square ribs in an open channel. The first half of the channel test section has straight parallel side walls, and each of the side walls of the second half of the test section converges linearly to produce the favorable pressure gradient. Two different values of half-angle ($\alpha = 1°$ and $2°$) of the converging side walls were used to vary the pressure gradient. For each value of α, transverse square ribs were glued onto the bottom wall both upstream of and within the converging sections. The pitch-to-height ratio of the ribs was varied to produce *d*-type, intermediate and *k*-type rib roughness. A particle image velocimetry was used to conduct detailed measurements over the ribs at several planes upstream of and within the converging sections. From these measurements, mean velocities and turbulent quantities were extracted at selected streamwise locations. The distributions of the mean velocities, turbulent intensities, and the mean and turbulent momentum fluxes at the interface between the rib cavities and the overlying boundary layer were used to provide insight into the interaction between the shear layers. The profiles of mean velocity, turbulent intensities, Reynolds shear stress and triple products were obtained to document the characteristics of favorable pressure gradient turbulent flow over square ribs in an open channel.

Keywords: Turbulent boundary layer; Open channel; Favorable pressure gradient; Particle image velocimetry; Transverse ribs

1. Introduction

Turbulent flow over rough surfaces has been studied extensively since Nikuradse (1933) performed his pioneer experiments over sand grains in a pipe. The roughness elements used include sand grains, gravels, wire mesh and perforated plates. Turbulent flows over two-dimensional transverse ribs have also been studied experimentally and in the recent past using large eddy simulations (LES) and direct numerical simulation (DNS). In this article, the rib height and pitch (which is defined as the distance between adjacent rib centers) will be denoted, respectively, by k and p. Following earlier experimental results (Perry et al., 1969; Tani, 1987), transverse ribs can be classified into *d*-type and *k*-type based on the pitch-to-height ratio, p/k. In this study, $p/k < 4$ is characterized as *d*-type and $p/k > 4$ as *k*-type ribs. Previous experimental studies include LDA measurements over *d*-type ($p/k = 2$) ribs in a zero pressure gradient (ZPG) turbulent boundary layer (Djenidi et al., 1999), and hot-wire measurements in a two-dimensional channel with both the top and bottom walls roughened by *k*-type ($p/k = 8$) ribs (Bakken et al., 2005). Cui et al. (2003) used LES to study turbulent flow over *d*-type, intermediated and *k*-type ribs in a two-dimensional channel, while Leonardi et al. (2003, 2005) performed DNS in two-dimensional channel over a wide range of p/k. Most of the earlier rough-wall studies are reviewed in the above references. Jiménez (2004) suggested that k/δ should be less than 0.025 in order to confine roughness effects to 50% of the logarithmic layer. However, the values of k/δ and k/h reported in most studies over transverse ribs are significantly higher than the limit proposed by Jiménez (2004). Connelly et al. (2006) conducted measurements over the range $0.009 \leqslant k/\delta \leqslant 0.063$ ($0.01 \leqslant k_s/\delta \leqslant 0.16$), where k_s is

* Corresponding author.
E-mail address: tachiemf@cc.umanitoba.ca (M.F. Tachie).

0142-727X/$ - see front matter © 2006 Elsevier Inc. All rights reserved.
doi:10.1016/j.ijheatfluidflow.2006.10.001

Nomenclature

C_f	skin friction coefficient
d_o	virtual origin
G	Clauser shape factor
h	water depth
H	boundary layer shape parameter
K	acceleration parameter
k	rib height
k_s	equivalent sand grain roughness height
p	pitch or distance between adjacent rib centers
P_k	production of turbulent kinetic energy
Re_h	Reynolds number based on freestream velocity and water depth
Re_θ	Reynolds number based on freestream velocity and momentum thickness
U	streamwise component of mean velocity
U_e	freestream velocity
U_τ	friction velocity
u, v	fluctuating velocity components in streamwise and transverse directions
$-uv$	Reynolds shear stress
u^3, u^2v, uv^2, v^3	triple products
w	gap between adjacent ribs
x, y, z	streamwise, transverse and spanwise coordinates

Greeks

α	half angle of channel's converging side walls
β	Clauser equilibrium parameter
δ	boundary layer thickness
δ^*	displacement thickness
κ	von Karman constant
ν	kinematic viscosity
θ	boundary layer momentum thickness
Δ	defect thickness
ΔB	roughness function
Π	Coles wake parameter

Subscript and superscript

$(\,)^+$	normalization by inner variables U_τ and ν

the equivalent sand grain roughness height, and concluded that the outer layer similarity in terms of the mean velocity is more robust than implied by Jiménez (2004). Previous rough wall studies demonstrate that wall roughness increases the friction drag, and the streamwise mean velocity profiles over rough walls are 'less full' compared to a smooth wall profile. Furthermore, the Reynolds stresses normalized by the freestream velocity or centerline velocity are higher over rough walls than on a smooth wall.

Favorable pressure gradient (FPG) or accelerating turbulent flows over a smooth wall have been studied in the past. For example, Blackwelder and Kovasznay (1972) obtained detailed measurements over a smooth wall in a converging channel with variable favorable pressure gradient. They found that the absolute values of the stresses were approximately constant along a mean streamline except in the immediate vicinity of the wall. Consequently, the values of u/U_e, v/U_e and $-uv/U_e^2$ decrease as the flow accelerates through the converging channel. Their results also indicate that the displacement and momentum thicknesses, and the Reynolds number based on momentum thickness decrease in the region prior to region of re-laminarization. The summary discussion provided above suggests that wall roughness and favorable pressure gradient have opposing effects on the profiles of mean velocity, turbulent intensities and Reynolds shear stress when normalized by the local freestream velocity. The goal of this paper is to study the characteristics of mild FPG turbulent flow over transverse square ribs in an open channel. The pitch-to-height ratio of the ribs was varied to produce *d*-type, intermediate and *k*-type rib roughness. A particle image velocimetry (PIV) was used to conduct velocity measurements over the ribs at several planes upstream of and within the converging sections. From these measurements, the mean velocities, turbulent intensities, Reynolds shear stress, triple products and turbulence production were obtained.

2. Scaling consideration for turbulent flow over smooth and rough walls

The mean velocity profiles over smooth and rough walls in ZPG turbulent boundary layers and fully developed channels have been analyzed in great detail (Millikan, 1938; Clauser, 1954 and Hama, 1954). For a rough wall turbulent boundary layer, a complete profile that describes the overlap and outer regions of the mean velocity may be written in the following form:

$$U^+ = \frac{1}{\kappa}\ln y^+ + C - \Delta B + \frac{2\Pi}{\kappa} f\left(\frac{y}{\delta}\right) \tag{1}$$

where $U^+ = U/U_\tau$, $y^+ = yU_\tau/\nu$, κ is the von Karman constant, C is a smooth wall constant, ΔB is the roughness function, Π is the Coles wake parameter, and f is a universal function of y/δ. Typical values of the log law constants are $\kappa = 0.41$ and $C = 5.0$. Note that $\Delta B = 0$ for a smooth wall. The sand grain roughness Reynolds number $k_s^+ = k_s U_\tau/\nu$, based on equivalent sand grain roughness height, k_s, is related to the roughness function as follows (Ligrani and Moffat, 1986):

$$\Delta B = \frac{1}{\kappa}\ln(k_s^+) + C - D \tag{2}$$

where $D = 8.5$. Schlichting (1979) proposed the following three roughness classifications: hydraulically smooth

($k_s^+ < 5$), transitionally rough ($5 \leqslant k_s^+ \leqslant 70$) and fully rough ($k_s^+ > 70$).

The outer region of the mean velocity is studied using the following mean velocity defect law:

$$U_e^+ - U^+ = f(y/\delta, \beta) \tag{3}$$

where $\beta = (\delta^*/\tau_w)(\mathrm{d}P_e/\mathrm{d}x)$ is the Clauser equilibrium parameter, and δ^* is the displacement thickness. Clauser demonstrated that a boundary layer with variable pressure gradient but constant β is in turbulent equilibrium. In this case, the gross properties can be scaled with a single characteristic length scale for which he proposed the defect thickness, $\Delta = \delta^*\lambda$, where $\lambda = [2/C_f]^{1/2} = U_e/U_\tau$. Clauser also defined a shape factor G, and suggested that G is a constant for an equilibrium boundary layer. The shape factor G and the Karman-type shape factor H are related by $G = \lambda(H-1)/H$. The expression for the defect thickness can be rearranged to produce $U_\tau/U_e = (\delta/\Delta)(\delta^*/\delta)$. Zagarola and Smits (1998) proposed that at a sufficiently high Reynolds number, $U_\tau/U_e \sim \delta^*/\delta$ for smooth wall turbulent boundary layers. This result implies that the ratio δ/Δ is invariant for general classes of turbulent boundary layers. Bergstrom et al. (2005) compiled a wide range of data sets obtained in ZPG turbulent boundary layers over a smooth surface, wire mesh, sand paper and perforated plates and observed that the analysis of Zagarola and Smits (1998) is also valid for rough walls. They proposed that the correlation, $C_f^{1/2} = 0.360\,(\delta^*/\delta)$, can be used to describe smooth and rough wall data obtained in ZPG turbulent boundary layers to within ±7% accuracy.

3. Experimental set-up and measurement procedure

3.1. Test sections

The experiments were performed in a re-circulation open channel flow. The test section of the main channel was 2500 mm long, 200 mm wide and 200 mm deep. Two different converging test sections made of 6 mm thick acrylic plates were inserted inside the main channel. Figs. 1a and b, respectively, show the side and top views of the inserted test section. The first 1250 mm of the insert had straight parallel side walls while each of the side walls of the remaining section converged linearly at an angle α. Two values of α ($\alpha = 1°$ and 2°) were studied. Transverse square ribs of size $k = 3$ mm were glued onto the bottom wall of the inserted test sections. As shown in Fig. 1, x co-ordinate is aligned with the streamwise direction, while y and z co-ordinates are, respectively, in the transverse and spanwise directions; $x = 0$ is at start of the converging

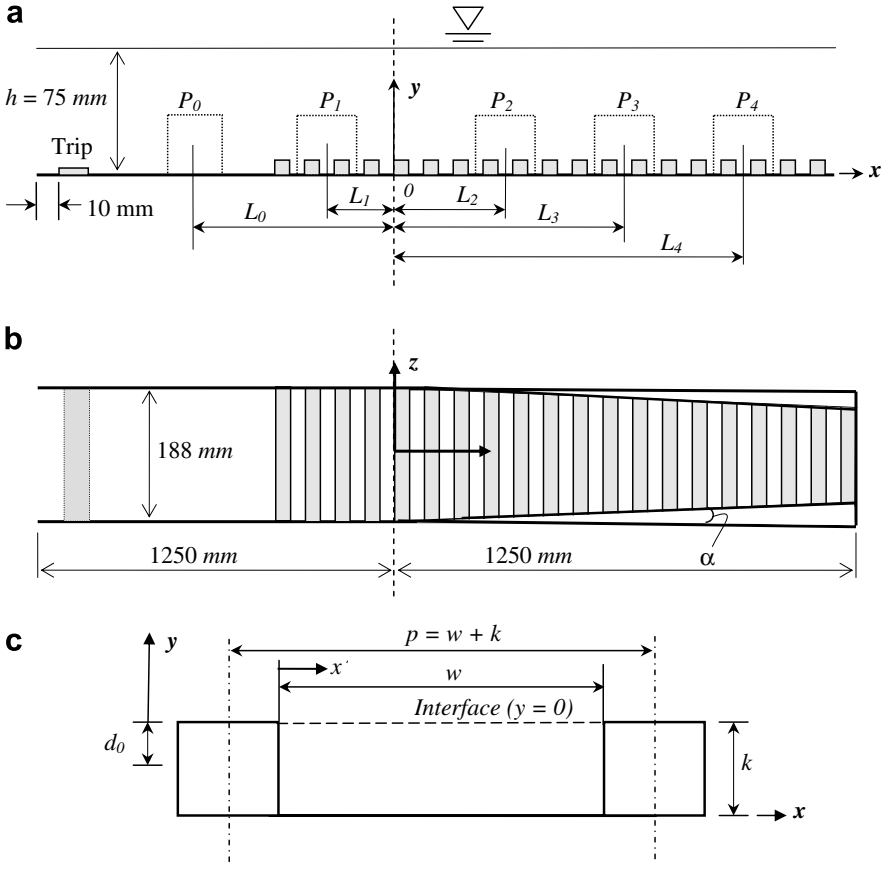

Fig. 1. Experimental setup (a) top view, (b) side view of the test section and (c) pitch and top plane of adjacent ribs. P_0–P_4 denoted x–y planes in which PIV measurements were made. L_0 is the x-location where smooth wall boundary layer measurements were made. L_1–L_4 correspond to cavity centers between ribs over which detailed data analysis was performed. $L_0 = -450$ mm, $L_1 = -125$ mm, $L_2 = 144$ mm, $L_3 = 432$ mm, $L_0 = 713$ mm.

section, $y = 0$ is at top plane of the ribs, and $z = 0$ is at the mid-plane of the channel. The length of ribs in the z-direction was varied to ensure that all the ribs span from one side wall to the other (Fig. 1b). In the x-direction, the ribs spanned 250 mm immediately upstream of the converging section and 800 mm into the converging section. Three pitch-to-height ratios, $p/k = 2$, 4 and 8, were used to study d-type, intermediate and k-type ribs, respectively. As shown in Fig. 1c, the virtual origin, d_o, is measured relative to the top plane of the ribs. Mean velocities will be denoted by upper case letters (e.g., U, V) while fluctuating quantities will be denoted by lower case letters (e.g., u, v, $-uv$, u^3, u^2v).

3.2. Measurement procedure

A PIV was used for the velocity measurements. The flow was seeded with 5 μm polyamide seeding particles. An Nd-YAG, 120 mJ pulse laser of 532 nm wavelength was used to illuminate the flow field. The laser sheet was located at the mid-plane of the channel. A 60 mm diameter Nikkor lens was fitted to 12-bits high-resolution digital camera (Dantec Dynamic HiSense 4M camera) that uses a CCD with 2048 pixels × 2048 pixels and a 7.4 μm pixel pitch. The measurements were made at a field of view of 69 mm × 69 mm. The instantaneous images were processed using the adaptive correlation option of FlowManager (version 4.50.17) developed by Dantec Dynamics. A 32 pixels × 32 pixels interrogation window (IW) with 50% overlap and moving average validation was used. The adaptive correlation uses a multi-pass FFT cross-correlation algorithm to determine the average particle image displacement within the IW. A three-point Gaussian curve fit was used to determine particle image displacement with sub-pixel accuracy. The mean velocity and turbulent statistics were calculated using a MATLAB script developed in our laboratory. Convergence test was performed by using $N = 1000$, 1500 and 2000 instantaneous images to compute the mean velocity and turbulent statistics. Fig. 2 shows that 2000 images are adequate. All results reported subsequently were obtained using 2000 images. Most of the images were re-processed using 32 pixels × 16 pixels with 50% overlap. The rationale was to evaluate the effect of IW size on the mean velocity and turbulent quantities. Typical data sets obtained from the two different IWs will be presented and discussed subsequently. Measurement uncertainty analysis was made following the AIAA standard derived and explained by Coleman and Steele (1995). In general, a complete uncertainty analysis involves identifying and quantifying both the bias and precision errors in each part of the measurement chain. In PIV technique, the accuracy of velocity measurement is limited by the accuracy of the sub-pixel interpolation of the displacement correlation peak. Other sources of measurement uncertainties include particle response to fluid motion, light sheet positioning, light pulse timing and size of interrogation area. Detailed analyses of bias and precision errors inherent in PIV technique are available in Prasad et al. (1992) and Forliti et al. (2000). Forliti et al. (2000) have shown that a Gaussian peak-fitting algorithm has the lowest bias and precision errors. On basis of the size of interrogation area and curve fitting algorithm used to calculate the instantaneous vector maps, and the large number of instantaneous images used to calculate the mean velocity and turbulent quantities, we estimate the uncertainty in the mean velocities at 95% confidence level to be ±2%. The uncertainties in turbulent intensities, Reynolds shear stress and triple products are estimated to be ±5%, ±10% and ±15%, respectively. Close to the ribs, uncertainties in mean velocities and Reynolds stresses are estimated to be ±2.5% and ±12.5%, respectively. In the graphs shown subsequently, error bars are used to indicate measurement uncertainty at 95% confidence level.

3.3. Test conditions

As shown in Fig. 1, boundary layer trips were located 100 mm downstream of the inlet section of the channel to ensure a rapid development of the boundary layer. In all the experiments, the water level was maintained at $h = 75 \pm 1.5$ mm along the test section. The volume flow rate was also kept constant in all experiments in order to maintain the upstream conditions as similar as possible. Measurements were made upstream of the converging section on the smooth floor in an x–y plane (denoted as P_0 in Fig. 1a) to characterize the approach boundary layer. Data sets were extracted specifically at $x\ (=L_0) = -450$ mm, and these data sets will hereafter be referred to as smooth (SM). The Reynolds number based on the water height and the approach freestream velocity on the smooth wall was $Re_h = 16{,}000$. The corresponding Froude number was $U_e/(gh)^{1/2} = 0.25$. Under these conditions, the free surface was calm, and no waves were observed. For each of the three rib types, reference velocity measurements were obtained upstream of the converging section in plane P_1. The plane was chosen to include 10 d-type ribs, 5 intermediate ribs and 3 k-type ribs. From this plane, data sets were extracted between two adjacent ribs whose cavity center was located at $x\ (=L_1) \approx -125$ mm. Because this plane was located upstream of the converging section where the side walls are parallel ($\alpha = 0$), the data sets over $p/k = 2$, 4 and 8 ribs will, respectively, be referred to as $R_2\alpha_0L_1$, $R_4\alpha_0L_1$ and $R_8\alpha_0L_1$, where $R = p/k$. For each rib type and slope, measurements were made at three x–y planes (P_2, P_3 and P_4) within the converging sections. For these planes, data sets were extracted between ribs whose cavity centers were located, respectively, at $x\ (=L_2) \approx 144$ mm, $x\ (=L_3) \approx 432$ mm, and $x\ (=L_4) \approx 713$ mm. For the d-type ribs, locations L_1, L_2, L_3 and L_4 correspond, respectively, to cavity centers between ribs 20 and 21, 65 and 66, 113 and 114, and 160 and 161. A total of 22 sets of 2000 instantaneous images were acquired. For convenience, the test conditions on the ribs will be denoted in the form $R_i\alpha_jL_k$, where R denotes pitch-to-height ratio ($i = 2$, 4, 8 for d-type,

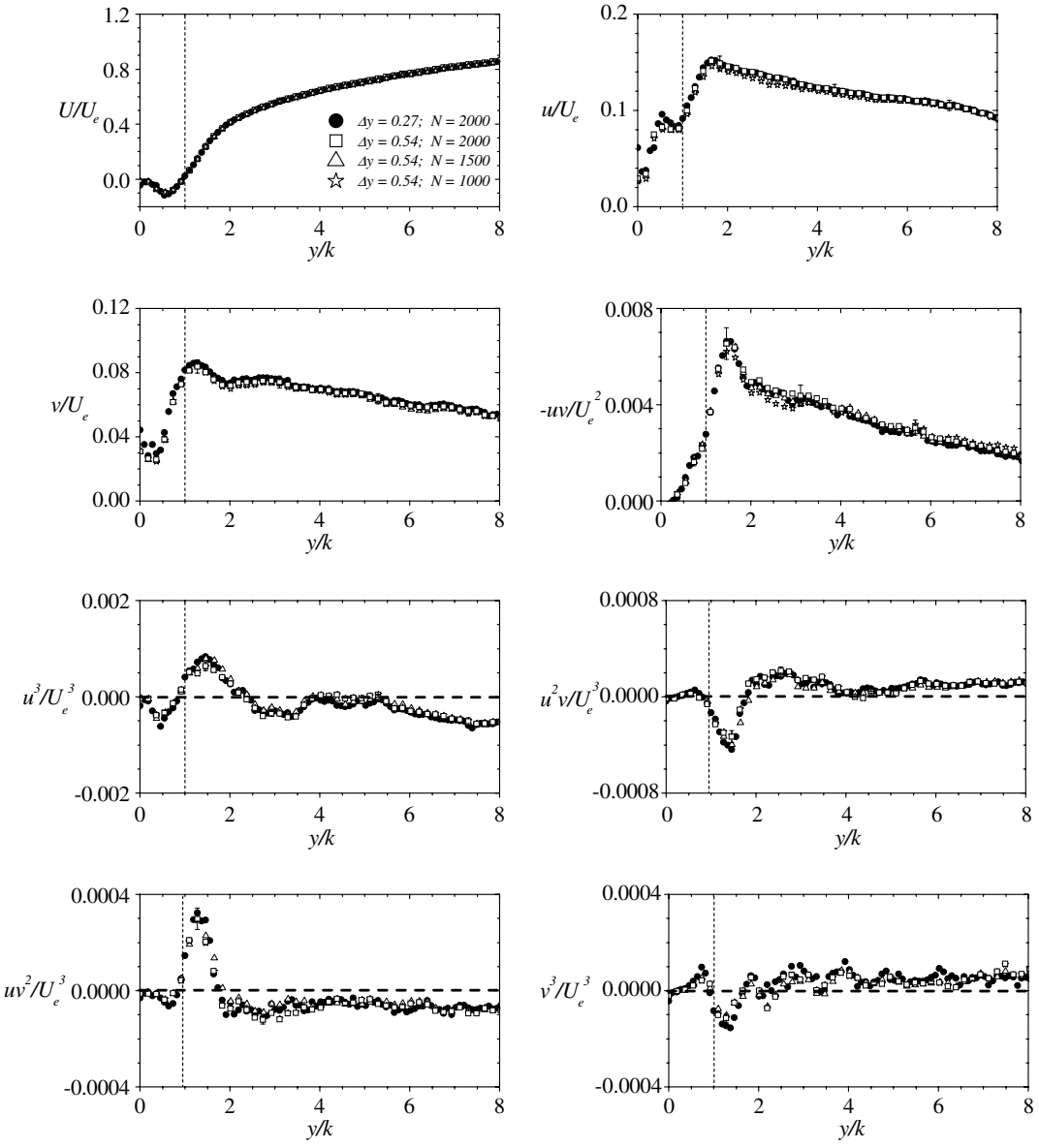

Fig. 2. Profiles of the mean velocity and turbulent quantities obtained using two IWs at the cavity center of test $R_4\alpha_1L_3$: (a) U, (b) u, (c) v, (d) $-uv$, (e) u^3, (f) u^2v and (f) uv^2. Each plot also shows profiles obtained using $N = 1000$, 1500 and 2000 instantaneous images. Error bars in this and subsequent figures denote measurement uncertainty at 95% confidence level.

intermediate and k-type, respectively), α is the half angle between the side walls ($j = 0$, 1, 2) and L is the rib center of interest in the nth plane ($k = 1$, 2, 3, 4). For example, $R_2\alpha_1L_3$ will denote measurements over d-type ribs ($R = 2$) within the $\alpha = 1°$ test section and at location $x = 432$ mm (L_3). Similarly, $R_8\alpha_0L_1$ will denote measurements obtained over k-type ribs ($R = 8$) and upstream of the converging section ($\alpha = 0$, and $x = -125$ mm (L_1)). The complete test conditions and various x-locations for which detailed data sets will be presented are summarized in Table 1. Table 1 also includes the corresponding freestream velocities, U_e, the boundary layer thicknesses, δ, and the Reynolds numbers based on the boundary layer momentum thickness, $Re_\theta = U_e\theta/\nu$. Note that for the rib surfaces, U_e is not a local value but a spatial averaged value. The spatial averaging was performed in the x-direction over a pitch, p. A spatial averaged profile typically corresponds to the average of 11, 22 and 44 individual profiles, respectively, for d-type, intermediate and k-type ribs. The spatial averaged profiles will be presented and discussed in later sections. Similarly, δ, δ^* and θ were determined from spatial averaged mean velocity profiles. The boundary layer thickness, δ, is defined as the y location where $U/U_e = 0.995$. Over the ribs, Re_θ increases as the flow accelerates through the converging section. The only exception is the d-type ribs in the $\alpha = 2°$ test section for which the value of Re_θ at L_4 ($R_2\alpha_2L_4$) is lower than at L_3 ($R_2\alpha_2L_3$). The ratio k/δ varied from 0.05 to 0.07 while the Reynolds number based on the rib height and the freestream velocity ($Re_k = U_ek/\nu$) varied from 720 to 1060. The present values of k/δ are higher than the limit

Table 1
Summary of test conditions

Test	p/k	α (°)	Plane	x (mm)	L	U_e (m/s)	δ (mm)	Re_θ
Smooth	–	0	P_0	−450	L_0	0.218	43	870
$R_2\alpha_0L_1$	2	0	P_1	−125	L_1	0.251	44	1050
$R_2\alpha_1L_3$	2	1	P_3	432	L_3	0.269	44	1200
$R_2\alpha_1L_4$	2	1	P_4	713	L_4	0.290	46	1370
$R_2\alpha_2L_3$	2	2	P_3	432	L_3	0.317	49	1750
$R_2\alpha_2L_4$	2	2	P_4	713	L_4	0.345	51	1670
$R_4\alpha_0L_1$	4	0	P_1	−125	L_1	0.254	44	1020
$R_4\alpha_1L_3$	4	1	P_3	432	L_3	0.283	49	1530
$R_4\alpha_1L_4$	4	1	P_4	713	L_4	0.314	47	1930
$R_4\alpha_2L_3$	4	2	P_3	432	L_3	0.302	50	1620
$R_4\alpha_2L_4$	4	2	P_4	713	L_4	0.355	53	2440
$R_8\alpha_0L_1$	8	0	P_1	−125	L_1	0.241	51	1410
$R_8\alpha_1L_3$	8	1	P_3	432	L_3	0.268	53	1780
$R_8\alpha_1L_4$	8	1	P_4	713	L_4	0.305	56	2300
$R_8\alpha_2L_3$	8	2	P_3	432	L_3	0.314	56	2160
$R_8\alpha_2L_4$	8	2	P_4	713	L_4	0.343	53	2350

proposed by Jiménez (2004); however, they are lower than those in many previous studies over ribs.

4. Results and discussion

4.1. Preliminary results

In this section, preliminary analyses to evaluate the effects of spatial resolution on the mean velocity and turbulent quantities are summarized. The streamlines over typical ribs and the mean velocities, turbulent intensities and momentum fluxes at the interface between the cavities and overlying boundary layer are reported. Finally, profiles of streamwise mean velocity and turbulent quantities obtained at rib and cavity centers within the roughness sublayer (which is defined as $y \leqslant 5k$) are used to show how these quantities vary close to the ribs.

4.1.1. Spatial resolution

The effects of spatial resolution on the mean velocity and turbulent quantities in near-wall turbulent flows have been studied using hot-wires (Johansson and Alfredsson, 1983) and downstream of backward facing step using a PIV (Piirto et al., 2003). These studies revealed that a relatively larger probe size or interrogation window side tends to underestimate the true values of the turbulent quantities in the wall region. As mentioned in Section 3.2, the PIV images were processed using two different IWs to evaluate any effects of spatial resolution on the flow statistics. Based on the friction velocity for the approach smooth wall boundary layer, the resolution for the two IWs was, respectively, 11.6×11.6 wall units and 11.6×5.8 wall units. With the 50% overlap used, the corresponding spacing between vectors or data points in the y-direction was $\Delta y = 0.54$ mm ($\Delta y^+ = 5.8$) and $\Delta y = 0.27$ mm ($\Delta y^+ = 2.9$). Fig. 2 shows that profiles of the mean velocity, turbulent intensities, Reynolds shear stress and triple products obtained from the two IWs are nearly indistinguishable. This implies that both IWs provide spatial resolutions that are adequate for these quantities above the top plane of the ribs. Data obtained for other test conditions are consistent with those shown in Fig. 2 but in some cases, the data sets from the lower resolution show less scatter. Saikrishnan et al. (2006) studied the effects of PIV resolution by comparing their PIV results obtained using different IWs with DNS data sets. The comparison was performed at $y^+ = 15$ (buffer region), $y^+ = 100$ (overlap region) and $y/\delta = 0.5$ (outer region). They observed that when $\Delta y^+ < 20$, the ratios of u^+, v^+ and $\langle -uv \rangle^+$ values obtained with the PIV at $y^+ = 15$ to the corresponding DNS values are 94% or higher. The peak values of u^+, v^+ and $\langle -uv \rangle^+$ obtained with the present PIV in the upstream *SM* test (Fig. 16) are consistent with values obtained from previous LDA measurement in an open channel (Tachie et al., 2003a). The 32×32 pixels and 32×16 pixels with 50% overlap produce, respectively, 127×127 and 127×255 data points (or vectors) in a plane. In the profiles to be presented subsequently, appropriate number of data points is skipped to minimize data congestion.

4.1.2. Streamlines

Streamlines were obtained for all test conditions to reveal some of the qualitative features of the mean flow pattern. These streamlines were calculated using 32×16 pixels with 50% overlap. This produced 11 vectors between the cavity floor and the top plane of the ribs ($y \leqslant k$). It was observed that for a particular rib type, streamlines obtained over the upstream ribs and those within the two converging sections ($\alpha = 1°$ and $\alpha = 2°$) are qualitatively similar. For this reason, only streamlines for Tests $R_2\alpha_1L_3$, $R_4\alpha_1L_3$ and $R_8\alpha_1L_3$ (corresponding to d-type, intermediate and k-type ribs in $\alpha = 1°$ channel in plane P_3) are shown in Fig. 3. The streamlines over the d-type and intermediate ribs reveal the well documented stable clockwise rotating vortices inside the cavities. The vortices fill the entire d-type and intermediate cavities and prevent the outer flow from reattaching onto the cavity floor. The streamlines are nearly parallel above the top plane of the d-type and intermediate ribs. For the intermediate ribs, a smaller corner counter-rotating vortex is also formed between the upstream rib and the primary vortex. For the k-type ribs, the outer flow penetrated into the cavity and reattached onto the floor at approximately $4k$ downstream of the rib center. Because several streamlines were skipped for clarity, the reattachment is not revealed in Fig. 3c. A primary clockwise rotating vortex occupied a significant fraction of the cavity (but not the entire cavity). Smaller counter rotating corner vortices are observed upstream of the downstream rib and downstream of the upstream rib (not shown). The streamlines are curved substantially close to the top plane of the k-type ribs indicating that flow over the k-type ribs is strongly inhomogeneous. They become nearly parallel at $y/k \approx 3$, which is within

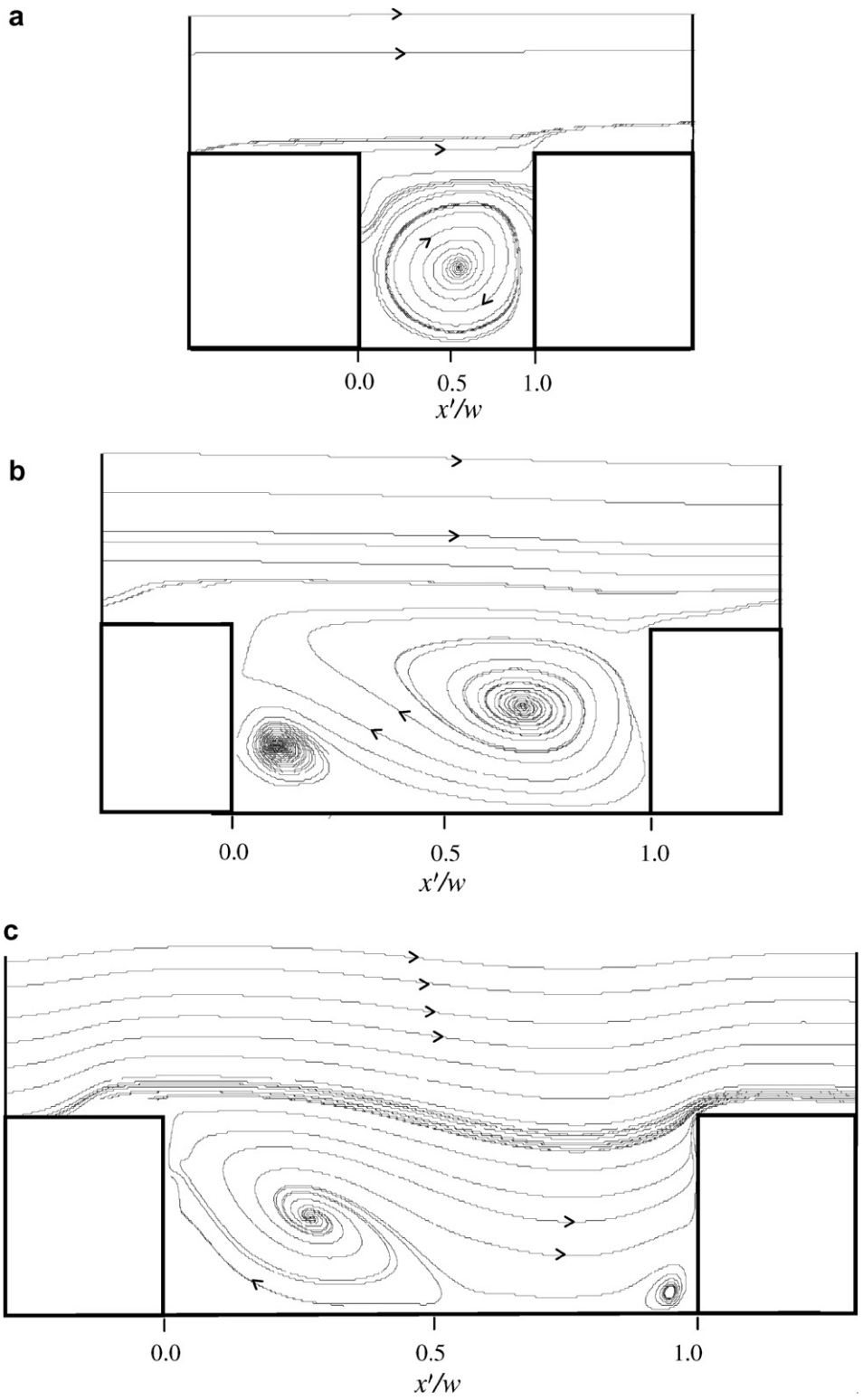

Fig. 3. Streamlines for selected test conditions: (a) $R_2\alpha_1L_3$, (b) $R_4\alpha_1L_3$ and (c) $R_8\alpha_1L_3$.

the roughness sublayer. The present results are qualitatively similar to observations made in previous studies conducted over transverse ribs in ZPG turbulent boundary layers and fully developed channels. It should be pointed out the k-type streamlines reported by Ashrafian et al. (2004) did not reattach onto the cavity floor. They attributed this to the low value of $k^+ = 13$ in their study. In the present study, k^+ values for the k-type ribs vary from 125 to 185. Results obtained from previous DNS and LES works revealed recirculation on the top of the ribs. These rib top recirculation zones are shallow and could not be resolved in the present study.

4.1.3. Mean velocities, turbulent intensities and momentum fluxes at interface

The mean velocities (U, V), turbulent intensities (u, v) and both the mean and turbulent momentum fluxes $(-UV, -uv)$ at the top plane of the ribs $(y = 0)$ were evaluated and are shown in Figs. 4 and 5. Since the top plane corresponds to the interface between the cavities and the overlying boundary layer, these data sets could provide insight into the interaction between the shear layers that developed within the cavity and the outer flow. The values of U and V obtained upstream of the converging section are shown, respectively, in Figs. 4a and c. In Figs. 4a and c, values of U and V obtained below $(y/k = -0.5)$ and/or above $(y/k = 1)$ the top plane are also included. Figs. 4a and c will be used to study the effects of rib type on the interaction between the cavity and the overlying boundary layer. The LDA results of Kameda et al. (2004) over 10 mm × 10 mm square ribs for $p/k = 4$ and 8 (star symbols in Figs. 4 and 5) in a ZPG turbulent boundary layer are also shown for comparison. Their values of k/δ varied from 0.15 to 0.19 which are 2–4 times as high as in the present study. The U and V values obtained at the top plane of the upstream ribs and those within the converging section at P_3 for $\alpha = 2°$ test sections are plotted together in Figs. 4b and d. These data sets will be used to study the effects of favorable pressure gradients on the interface values.

For a similar p/k, the present and previous data sets show identical trends along the interface, however, the magnitude of the previous data is higher than in the present work. At the interface, the flow accelerates $(\partial U/\partial x > 0)$ in the region adjacent to the upstream ribs and decelerates $(\partial U/\partial x < 0)$ in the region adjacent to the downstream ribs. As a result, the normal production term $-u^2\partial U/\partial x$ in the turbulent kinetic energy transport equation will be negative close to the upstream rib and positive adjacent to the downstream rib. This implies that the normal production term will augment turbulence production close to the downstream ribs but decrease production close to the upstream ribs. The magnitude of U values below the interface $(y/k = -0.5)$ is ordinarily small, especially inside the

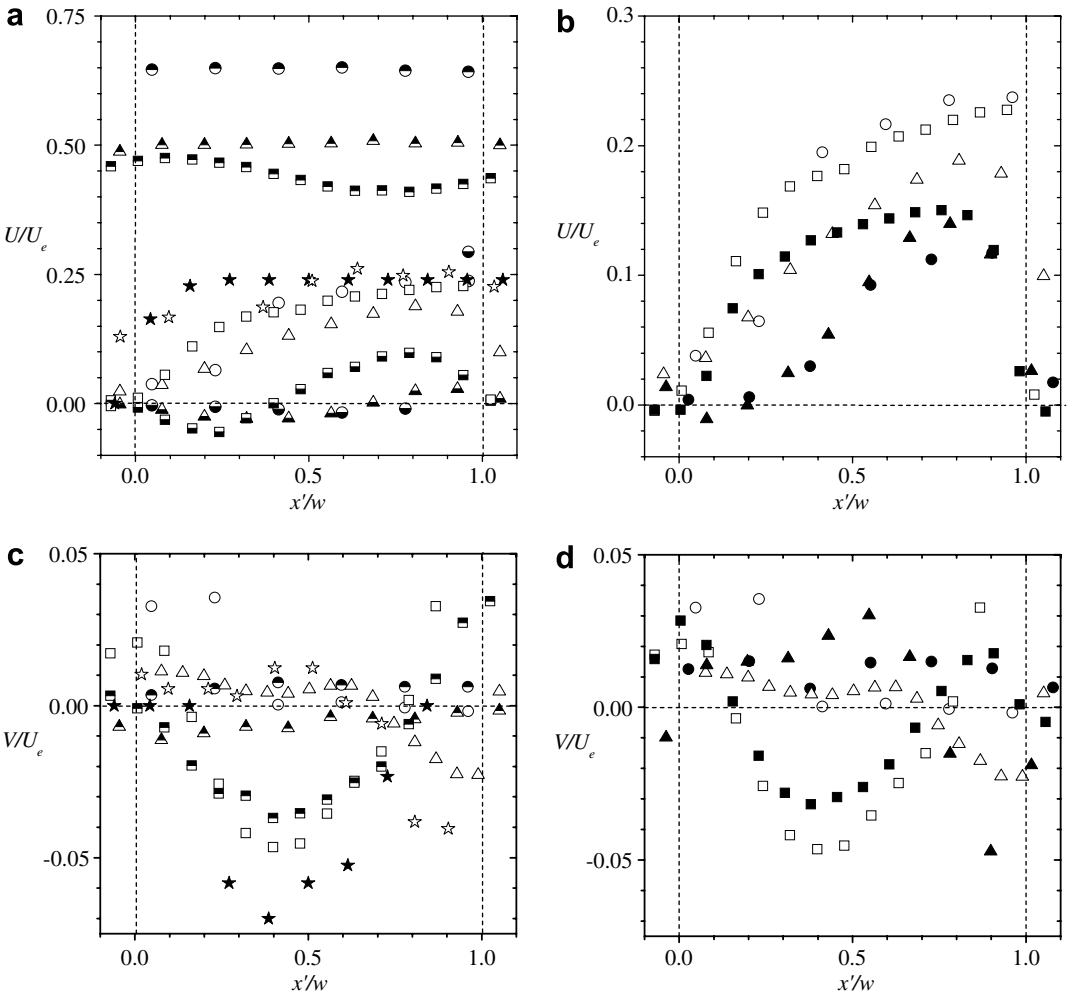

Fig. 4. The mean velocities near the interface. The symbols are: $R_2\alpha_0L_1$: $y/k = -0.5$ (◒); $y/k = 0$ (○); $y/k = 1$ (◓); $R_4\alpha_0L_1$: $y/k = -0.5$ (▲); $y/k = 0$ (△); $y/k = 1$ (▲); $R_8\alpha_0L_1$: $y/k = -0.5$ (⬓); $y/k = 0$ (□); $y/k = 1$ (⬒); $R_2\alpha_2L_3$ (●); $R_4\alpha_2L_3$ (▲); $R_8\alpha_2L_3$ (■); LDA data by Kameda et al. (2004): $p/k = 4$ (☆) and $p/k = 8$ (★).

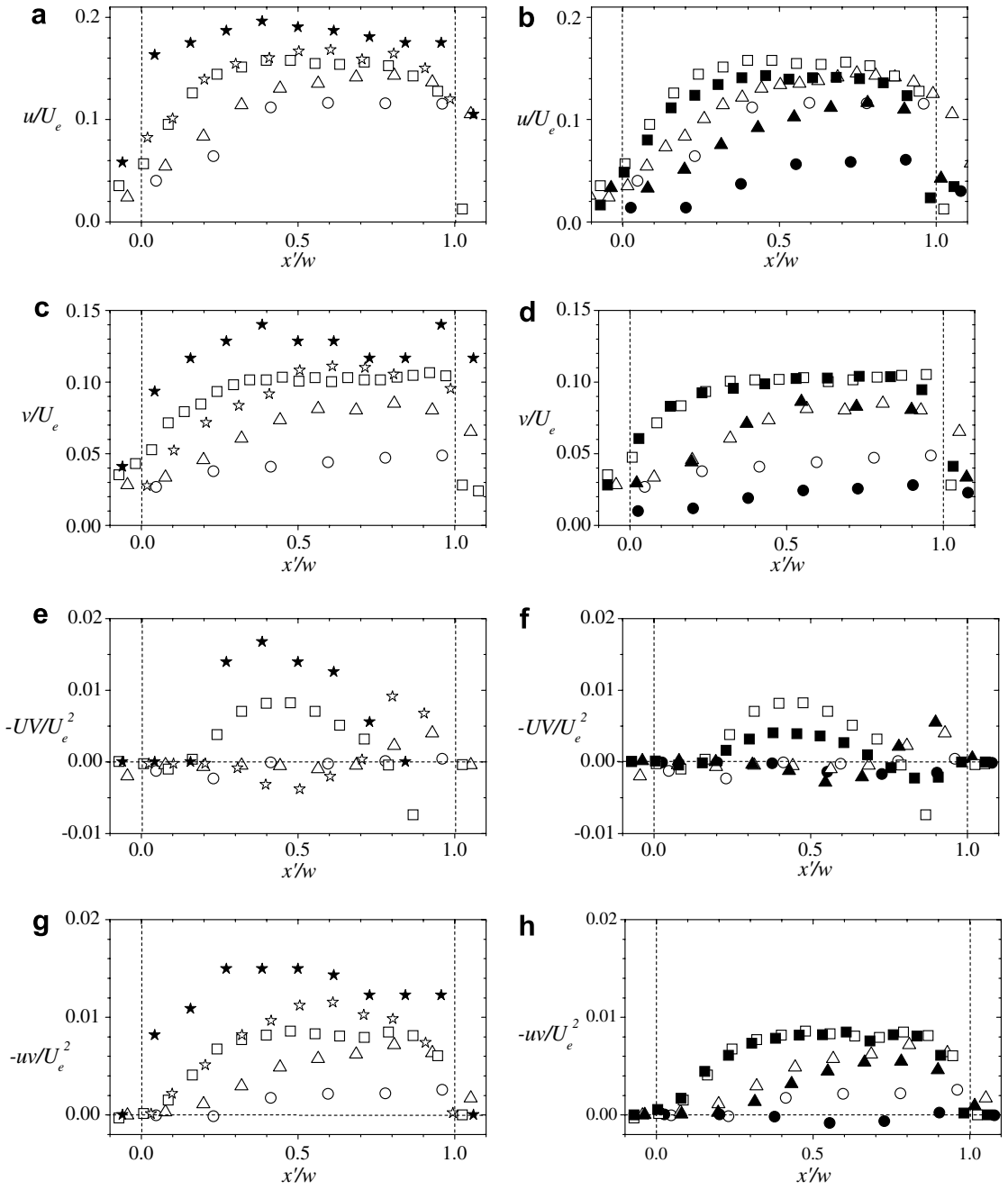

Fig. 5. Turbulent intensities and mean and turbulent momentum fluxes near the interface. Symbols as in Fig. 4.

d-type and intermediate cavities. Negative values of U are found in the cavities indicating flow reversal. At the particular y location shown, the magnitude of flow reversal increases with pitch ratio. Fig. 4a also reveals that the shear layer develops most rapidly across the *d*-type ribs and least across the *k*-type ribs. This observation is based on the premise that $\partial U/\partial y$ is typically largest across the *d*-type interface and smallest across the *k*-type interface. For example, at cavity center ($x'/w = 0.5$), U/U_e increases from nearly 0 at $y/k = -0.5$ to 0.65 at $y/k = 1$ across the *d*-type interface. Over the same y-range and at cavity center, U/U_e increases from 0 to 0.5 across the intermediate interface and 0.04 to 0.42 across the *k*-type interface. At the *k*-type interface, values of U for $\alpha = 1°$ test section (not shown) are similar to the upstream values but those obtained in the $\alpha = 2°$ test section are lower. For *d*-type and intermediate ribs, U values decrease as α increases.

The V profiles are closely related to the pitch ratio in response to the curvature of the streamlines shown in Fig. 3 (Kameda et al., 2004). At $y/k = 1$, values of V over the *d*-type and intermediate ribs are, respectively, positive and negative, and for both rib types, the magnitudes of V are less than 1% of the freestream velocity. At the same location, and along the *k*-type ribs, V is predominantly

negative with magnitude as high as 3.5% of the freestream velocity. At the interface of each of the three rib types, V takes positive values in the region adjacent to the upstream ribs. It is clear from the figure that vertical motion across the k-type interface is substantially higher than across the d-type and intermediate type interface. This would likely produce a stronger interaction between the overlying boundary layer and the k-type cavities than the d-type and intermediate type cavities.

The streamwise and transverse turbulent intensities (Figs. 5a–d) increase immediately downstream of the upstream ribs to a maximum value and then decrease to no-slip value on the downstream rib. The turbulent intensities develop more rapidly to their respective maximum values along the k-type ribs than along the d-type and intermediate interface. The values of u and v along the interface also increase substantially with pitch ratio. Figs. 5b and d show that the turbulent intensities along the k-type interface do not show any systematic trend with flow acceleration (i.e., higher α and L values). For d-type, on the other hand, values of u and v decrease with increasing flow acceleration. The mean and turbulent momentum fluxes ($-UV$ and $-uv$) at the interface are shown in Figs. 5e–h. The mean momentum flux is produced by streamline curvature (Kameda et al., 2004). The large streamline curvature observed over the k-type ribs produces relatively larger values of $-UV$ while the near parallel streamlines over the d-type and intermediate ribs produce very little momentum flux. Since momentum fluxes at the interface are related to momentum transport between the cavities and the overlying boundary layer, the non-zero values of $-UV$ and $-uv$ in these figures are indicative of momentum exchange between the cavities and the overlying boundary layer. The values of $-uv$ at the k-type interface are similarly larger than those obtained over the d-type and intermediate ribs. One may conclude from these figures that the interaction between the cavities and overlying boundary layer is strongest for the k-type and least for the d-type ribs. The enhanced interaction between the shear layers along the k-type ribs may explain the higher turbulent intensities observed over the k-type ribs compared to the d-type ribs. Over most of the k-type ribs, the magnitudes of $-UV$ values are similar or higher than $-uv$ values. The DNS results of Ashrafian et al. (2004) over $p/k = 8$ square ribs showed that $-UV$ exceeds twice the value of $-uv$ immediately above the rib crest so that the dynamical importance of $-UV$ cannot be neglected close to k-type ribs. Their results also reveal that the mean velocities become uncorrelated a short distance above the ribs. For d-type and intermediate ribs, on the other hand, values of $-uv$ are generally higher than $-UV$ and so the mean momentum flux is not expected to play a significant role in momentum transport across these interfaces. The turbulent momentum fluxes do not show any systematic trend with flow acceleration over the intermediate and k-type ribs; however, they decrease with increasing flow acceleration over the d-type ribs.

4.1.4. Mean velocity and turbulent quantities in the roughness sublayer

The profiles of U, u, v and $-uv$ obtained at the rib and cavity centers for some selected test conditions are shown in Fig. 6. For the d-type and intermediate ribs, the various profiles obtained at the rib and cavity centers are nearly indistinguishable above the top plane of the ribs ($y/k > 0$). The magnitude of back flow velocity at cavity centers is approximately 2% of the freestream velocity for d-type and 4% for intermediate. The cavity center of the k-type rib is located around the reattachment point and so the U profile at this location does not reveal large negative values. Differences are observed in the k-type profiles which are probably due to the stronger interaction between the cavity flow and outer flow discussed in Section 4.1.3. These differences are, however, limited to $y < 3k$ which is well inside the roughness sublayer.

4.2. Effects of rib type and flow acceleration

In this section, the spatial averaged profiles are used to study the effects of rib type and flow acceleration on the boundary layer characteristics, mean velocity profiles, turbulent intensities and Reynolds shear stress.

4.2.1. Boundary layer characteristics

The local freestream velocity U_e^* obtained at selected x locations over the smooth wall (P_0), upstream ribs (P_1), and over the ribs within the converging sections (P_2, P_3 and P_4) are shown in Fig. 7a. The corresponding spatial averaged values U_e are shown in Fig. 7b and in Table 1. The values of U_e^* and U_e measured over the upstream ribs (P_1) are typically 10–16% higher than the smooth wall values. This increase is partly due to reduction of flow area by the ribs. The freestream velocities increase monotonically in the converging section ($x > 0$). At corresponding x-locations inside the converging section, values of U_e^* and U_e obtained in $\alpha = 2°$ test section are 10–20% higher than in the $\alpha = 1°$ test section. The freestream velocity at the start of the converging section ($x = 0$) is approximately 0.25 m/s. Note, however, that the freestream velocities over the k-type ribs just upstream of the converging section is somewhat lower than 0.25 m/s. The dash and solid lines in Fig. 7a and b show how the mean velocity would have varied in the converging sections (assuming freestream velocity of 0.25 m/s at $x = 0$) if the flow were inviscid and there were no cavities. Because of boundary layer growth over the ribs and on the side walls of the channel, the experimental values (symbols) are higher than the ideal values (lines). The increase in U_e along the converging section is not exactly linear. However, in estimating the gradient $\mathrm{d}U_e/\mathrm{d}x$ from the measured data in each measurement plane, a linear variation of U_e with x was assumed and $\mathrm{d}U_e/\mathrm{d}x$ was evaluated as the slope of a least square linear fit to U_e versus x. The values of the gradient $\mathrm{d}U_e/\mathrm{d}x$, acceleration parameter $K = (\nu/U_e^2)(\mathrm{d}U_e/\mathrm{d}x)$, and the absolute values of the Clauser equilibrium parameter, β, are shown

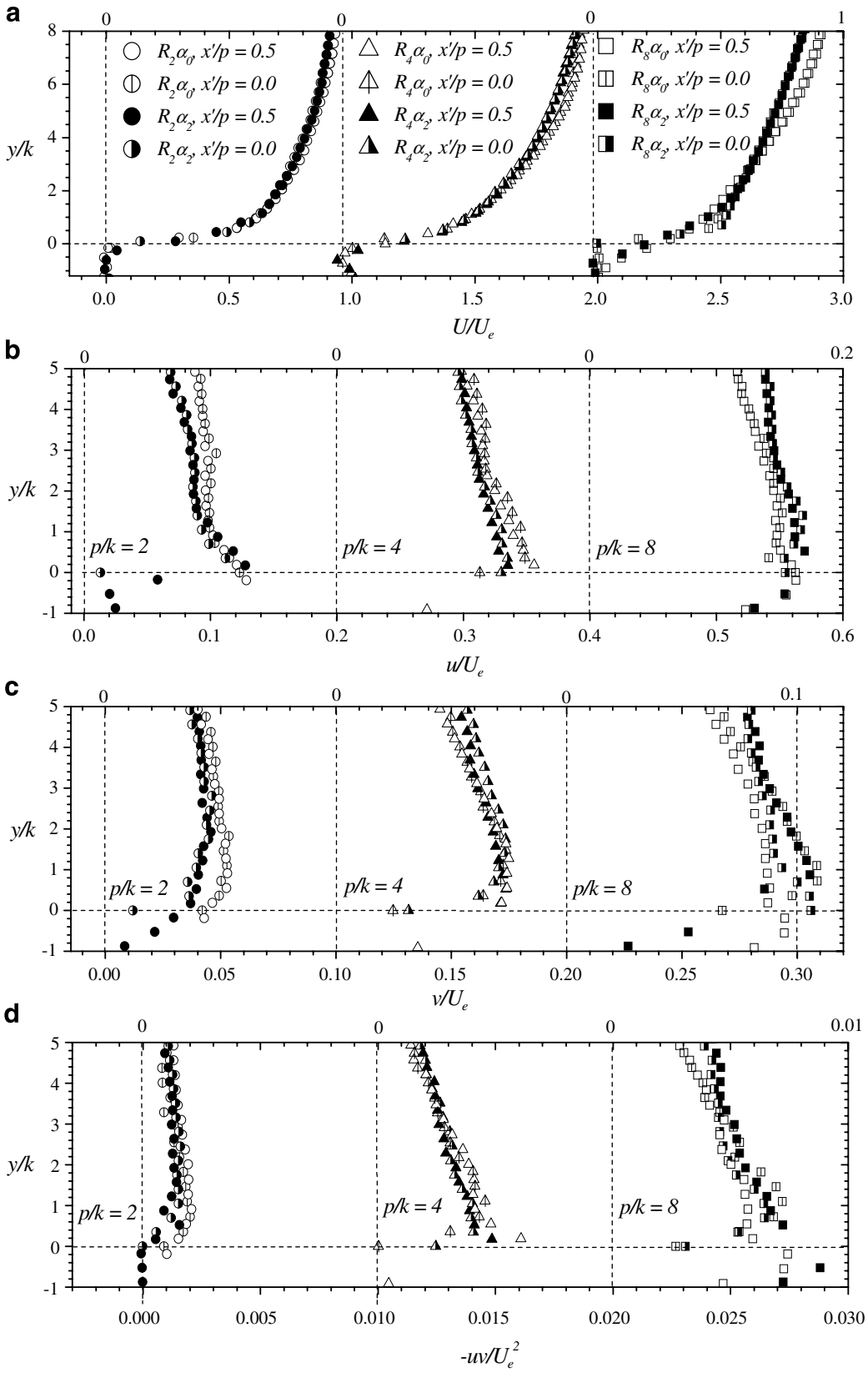

Fig. 6. Comparison between profiles obtained at the rib and cavity centers within the roughness sublayer: (a) streamwise mean velocity, (b) streamwise turbulent intensity, (c) transverse turbulent intensity and (d) Reynolds shear stress.

in Figs. 7c, d and e, respectively. The values of dU_e/dx and K over the smooth wall are non-zero indicating a small but non-negligible acceleration of the approach boundary layer. The values of dU_e/dx, K and β over the upstream ribs

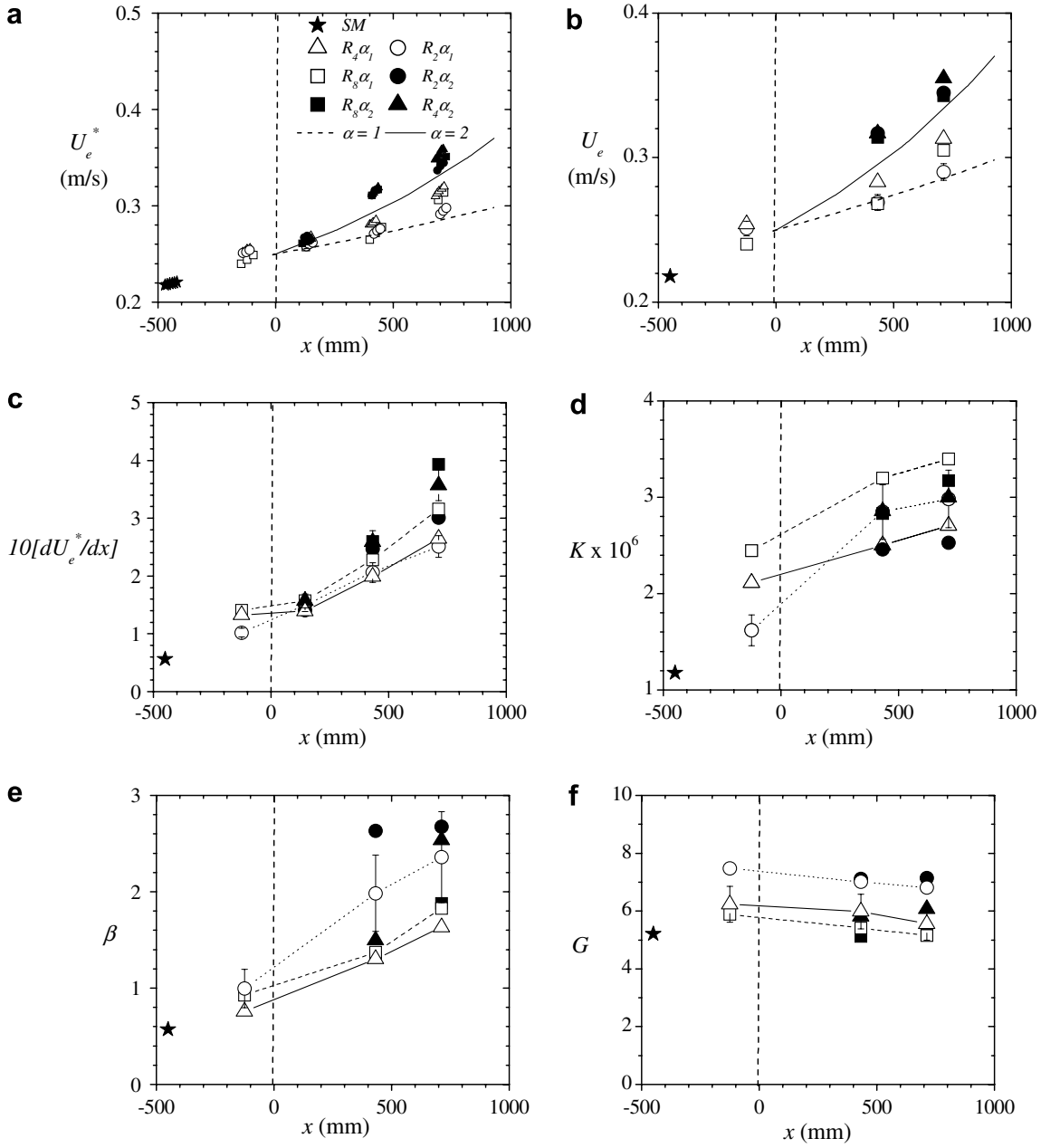

Fig. 7. Various mean flow parameters obtained upstream of and within the converging section: (a) local freestream velocity, (b) spatial averaged freestream velocity, (c) velocity gradient, (d) acceleration parameter, (e) absolute values of Clauser equilibrium parameter and (f) Clauser shape factor. Lines in (c)–(f) are for visual aid only.

are higher than the corresponding smooth wall values. Flow acceleration is more rapid in the $\alpha = 2°$ test section than in the $\alpha = 1°$ test section. The figures show a modest increase in K and β along the converging sections but the increase is of the order of measurement uncertainty. The variation of the shape factor G is shown in Fig. 7f. The value of $G = 5.2$ obtained in the approach smooth wall boundary layer is lower than typical values of 6.1 and 6.3 reported in ZPG turbulent boundary layers. It is not clear if the present low value is due to the moderate FPG and characteristic high background turbulence levels. Rib roughness increased the value of G to about 6–7.2 in the upstream section. The values of G reported in earlier ZPG over rough walls vary from study to study. The data reported by Bandyopadhyay (1987) suggest $G = 6.1$ for both smooth and rough walls. Furuya and Fujita (1967) obtained values of $G = 6.3$ and 7, respectively, for smooth and rough walls.

The variation of the displacement thickness, δ^*, momentum thickness, θ, shape factor, $H\ (=\delta^*/\theta)$, and defect thickness, Δ, along the channels is shown in Fig. 8. The values of δ^* and θ are higher over the ribs than on the smooth wall. This is indicative of the characteristic higher mass and momentum flux deficit associated with rib roughness. Over the ribs, the values of δ^* and θ are highest for the k-type ribs. The values of δ^* and θ obtained in the $\alpha = 1°$ test sec-

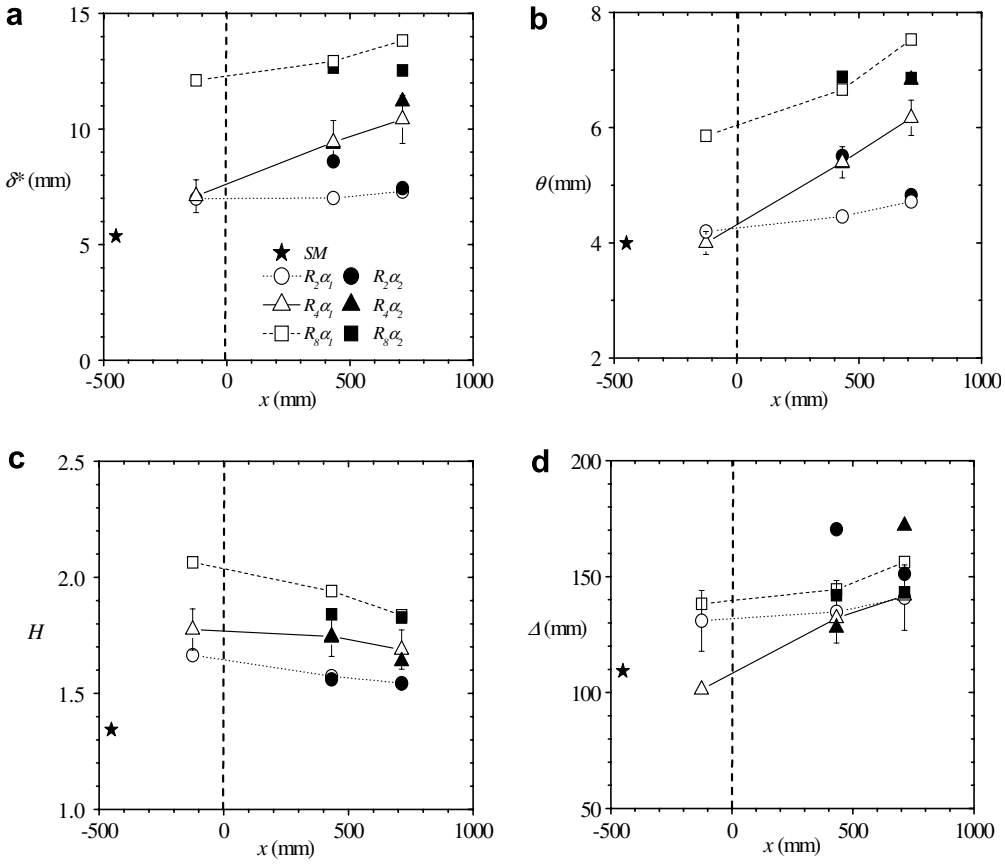

Fig. 8. Boundary layer parameters obtained from spatial averaged mean velocity profiles at selected locations upstream of and within the converging section: (a) displacement thickness, (b) momentum thickness, (c) shape factor and (d) defect thickness. Lines are for visual aid only.

tion (open symbols) increase monotonically with x. This is similar to observations made, for example, by Smalley et al. (2001) and Bandyopadhyay (1987) in ZPG turbulent boundary layer developing over transverse ribs. It appears the gentle slope ($\alpha = 1°$) does not affect the boundary layer characteristics significantly. For the larger slope ($\alpha = 2°$), values of δ^* and θ over d-type ribs at L_4 are lower than at L_3 while values of δ^* and θ increase over the intermediate roughness and remain nearly constant over the k-type ribs. The trend observed over the d-type ribs in the $\alpha = 2°$ test section is similar to results obtained in accelerating flow over a smooth wall (Blackwelder and Kovasznay, 1972). Since δ^* and θ are related to mass and momentum deficit within the boundary layer, Figs. 8a and b imply that ribs are more effective in enhancing mass flux deficit than momentum flux deficit. For example, the increase in δ^* compared to the smooth wall value is 30–60% for d-type, 30–100% for intermediate, and 125–160% for k-type ribs. Corresponding increase in θ is only 5–37% for d-type, 2–70% for intermediate, and 47–90% for k-type ribs. As a result, the shape factor H is higher for the ribs than for the smooth wall (Fig. 8c). Connelly et al. (2006) also reported higher increase in δ^* (31–126%) than in θ (13–46%) for measurements over sand papers and wire mesh. The value of $H = 1.34$ for the smooth wall flow is similar to previous open channel results at similar Reynolds numbers (Tachie et al., 2003b). The upstream ribs increased the value of H to 1.66 (d-type), 1.78 (intermediate) and 2.06 (k-type). This is followed by a gradual decrease in H as the flow evolves through the converging section. The decrease in values of H over the ribs in the converging section implies that flow acceleration diminishes the effectiveness of the rib roughness to enhance mass flux deficit in comparison to momentum deficit. Fig. 8d shows that the defect thickness Δ increases along the channel but no systematic effects of rib type are observed.

4.2.2. Mean velocity profiles in outer coordinates

The development of the spatial averaged streamwise mean velocity profile over the ribs is shown in Fig. 9a using outer scaling (U_e and δ). In this plot, profiles obtained upstream of and within the converging sections over a particular rib type are plotted together. Note that values of U/U_e vary from 0 to 1, and the horizontal axis is staggered. For d-type, the profiles obtained in the converging section are nearly independent of α. The d-type profiles at L_3 collapse reasonably well on the upstream profile. Further downstream (L_4) the profiles become 'more full' than the upstream profile. This is similar to trends observed in accelerating flows over a smooth wall. In contrast, the profiles obtained in the converging section over the intermediate and k-type ribs are generally 'less full' in comparison to

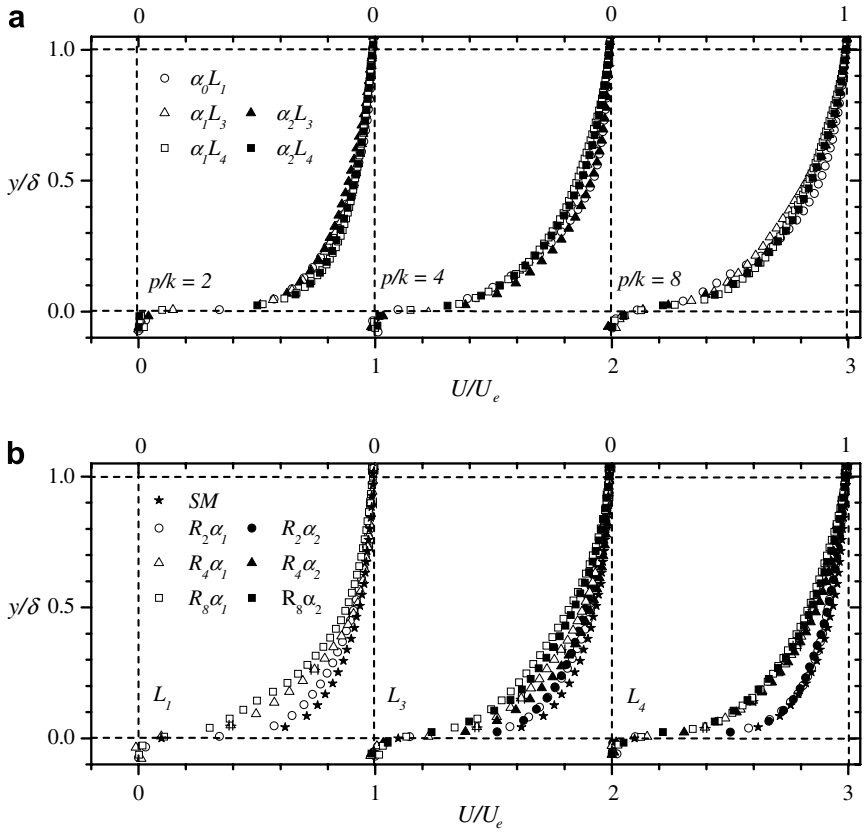

Fig. 9. The spatial averaged streamwise mean velocity profiles over the ribs in outer coordinates.

the upstream profile. The profiles obtained over the three rib types at L_1, L_3 and L_4 are shown in Fig. 9b to demonstrate the effects of rib type on the mean velocity profile at similar streamwise locations. Because of the enhanced drag characteristics of the ribs, the rib profiles are less full in comparison to the smooth profile. The *k*-type profiles show the greatest deviation from the smooth wall profile due to the higher drag characteristics of the *k*-type ribs. The profiles over the *d*-type are only marginally different from the smooth wall profile, and at the last measurement station (L_4) the *d*-type and smooth wall profiles are nearly indistinguishable. Therefore, the mean velocity profile over *d*-type rib resembles the smooth-wall profile except for a displaced y and an increase in U_e associated with flow blockage by the ribs. Cui et al. (2003) also made a similar observation in their study. The profiles over the *k*-type ribs do not vary significantly within the converging section. At location L_1, the intermediate and *k*-type profiles are not significantly different. The intermediate profiles become less full and approach *d*-type profiles at L_3 but tend to collapse reasonably well onto the *k*-type profiles at L_4.

4.2.3. Friction velocity and mean velocity profiles in inner coordinates

An accurate determination of the friction velocity, U_τ, over ribs and other rough walls remains a challenging task because the virtual origin, d_o, and roughness function, ΔB, are not known a priori. Previous LES and DNS results over ribs show that the overlap region of the spatial averaged mean velocity is well described by the classical log law. The log law is also valid for open channel flows and mild to moderate favorable pressure gradient turbulent flows. The universal log law is assumed to be valid for all the present test conditions. In this study, we employ a methodology that is similar to the one used by Smalley et al. (2001) in determining U_τ over transverse ribs in ZPG turbulent boundary layer. The method assumes existence of a constant stress region. In this region, the Reynolds shear stress has a plateau, $-uv_p$. An estimate of U_τ was obtained from $U_\tau = [-uv_p]^{1/2}$. With this estimate, the dimensionless mean velocity profile (U^+ versus y^+) was plotted in a semi-logarithmic format. Note that for the ribs, y is defined to include d_o (i.e., $y + d_o$). The values of d_o and U_τ were varied in a trial-and-error process until optimized values of d_o and U_τ were obtained that gave a straight line with the right slope ($\kappa = 0.41$). For the smooth wall, data in the range $y^+ = 30$ to $y/\delta = 0.5$ were used in the least square fit to the log law because of the negligible wake (Fig. 10a). For the rib surfaces, data in region $y^+ > 30$ and $y/\delta < 0.2$ were used, however, the exact y range varies from rib type to rib type, and from location to location due to the varying nature of the strength of the wake (Fig. 10). The optimized U_τ values are summarized in Table 2. These values are higher than the initial estimates. For example, the optimized U_τ is 10% higher for smooth, and typically 15% higher for *d*-type, 7% higher for intermediate, and

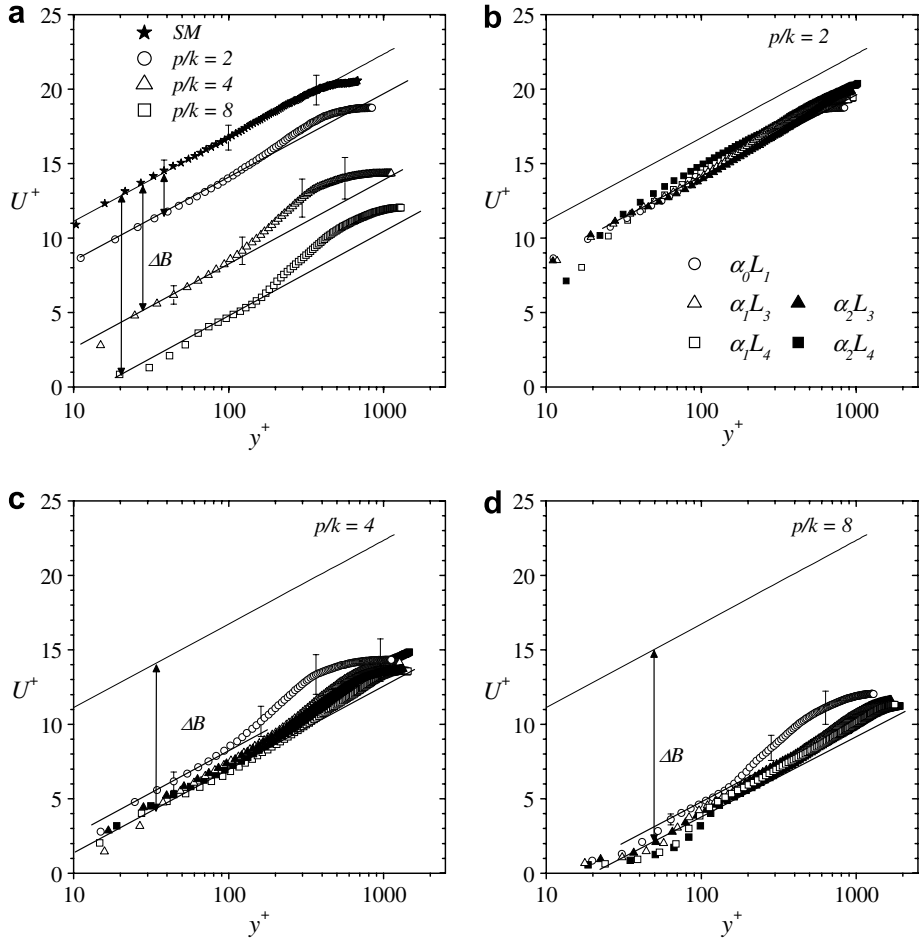

Fig. 10. The spatial averaged streamwise mean velocity profiles over the smooth wall and ribs in inner coordinates.

Table 2
Summary of boundary layer and drag characteristics

Test	Re_θ	d_o/k	U_τ (mm/s)	ΔU^+	U_τ/U_e	Π	k_s^+	k_s/k	k_s/δ	δ/Δ
Smooth	870	–	10.6	–	0.048	0.02	–	–	–	0.395
$R_2\alpha_0L_1$	1050	0.09	13.4	2.2	0.053	0.21	10	0.23	1.6	0.336
$R_2\alpha_1L_3$	1200	0.10	14.1	2.1	0.052	0.12	10	0.24	1.6	0.326
$R_2\alpha_1L_4$	1370	0.11	15.0	1.8	0.050	0.04	11	0.20	1.3	0.329
$R_2\alpha_2L_3$	1750	0.05	16.2	2.3	0.052	0.14	9	0.29	1.8	0.288
$R_2\alpha_2L_4$	1670	0.09	17.2	1.4	0.049	0.02	8	0.14	0.8	0.338
$R_4\alpha_0L_1$	1020	0.27	17.8	8.0	0.070	0.41	110	2.07	14.1	0.435
$R_4\alpha_1L_3$	1530	0.26	20.2	8.7	0.071	0.27	149	2.50	15.3	0.372
$R_4\alpha_1L_4$	1930	0.21	23.1	9.3	0.073	0.18	190	2.77	17.7	0.331
$R_4\alpha_2L_3$	1620	0.25	22.1	8.9	0.073	0.18	161	2.43	14.5	0.391
$R_4\alpha_2L_4$	2440	0.26	24.2	9.0	0.068	0.21	168	2.33	13.2	0.308
$R_8\alpha_0L_1$	1410	0.50	21.1	11.5	0.088	0.41	480	8.00	47.1	0.369
$R_8\alpha_1L_3$	1780	0.43	24.2	11.8	0.090	0.21	530	7.37	41.7	0.368
$R_8\alpha_1L_4$	2300	0.48	27.0	11.8	0.089	0.10	530	6.53	35.0	0.358
$R_8\alpha_2L_3$	2160	0.44	27.1	11.8	0.086	0.15	530	6.53	35.0	0.394
$R_8\alpha_2L_4$	2350	0.55	30.5	12.2	0.089	0.14	620	6.77	38.3	0.370

4% higher for k-type ribs. Smalley et al. (2001) reported a 4% difference between the estimated and optimized U_τ values. Connelly et al. (2006) remarked that U_τ values determined from Clauser plot technique are typical 5% higher than values determined from the total stress method, irrespective of the specific surface roughness. It will be shown later that in the inner region, profiles of $-uv$ fall more rapidly from their peak values in FPG flows than observed in ZPG. As a result the plateau is not always as blunt and distinct as observed in high Reynolds number ZPG turbulent boundary layers. This may introduce an error in the estimated U_τ values. For a low Reynolds number turbulent

flow over a smooth wall, the viscous contribution ($\nu\partial U/\partial y$) to the total stress cannot be neglected in the wall region. In fact, prior DNS and measurements in ZPG, fully developed channel and open channel flow show that $(-u^+v^+)_{max} < 1$ at low Reynolds numbers. Therefore, the differences observed in the estimated and optimized U_τ values for the smooth wall may be partly due to low Reynolds number effects. The *d*-type ribs are in the transitionally rough regime (Table 2). Previous studies indicate that for ribs with $p/k = 2$, the viscous contribution to the total drag may be up to 50–70% (Leonardi et al., 2003; Kameda et al., 2004). Since the Reynolds shear stress and viscous drag depend on Reynolds number, the differences in the estimated and optimized values over the *d*-type ribs may also be partly explained by low Reynolds number effect. Another possible explanation for the differences in the estimated and optimized U_τ values for the ribs is that the spatial averaged values of $-UV$ are small but non-zero close to the rib interface. Their contributions to the wall shear stress may not be negligible. The measurement uncertainty in U_τ is difficult to quantify for rough walls. Here, it is estimated to be of the order of 5% for the smooth wall and 10% for the ribs.

Table 2 shows that the ratio d_o/k varies significantly from one rib type to the other but nearly independent of slope and streamwise location for a particular rib type. This variation reflects the varying degree of interaction between the outer flow and cavities of the different rib types. The values of d_o/k for the *d*-type, intermediate and *k*-type ribs are, respectively, 0.09 ± 0.02, 0.25 ± 0.02 and 0.48 ± 0.05. These values are in reasonable agreement with $d_o/k = 0.05$ (for $p/k = 2$), 0.35 (for $p/k = 4$) and 0.50 (for $p/k = 8$) obtained in the DNS work by Leonardi et al. (2003). They are somewhat lower than values of $d_o/k = 0.28$ ($p/k = 2$), 0.47 ($p/k = 5$) and 0.72 ($p/k = 10$) in the LES work by Cui et al. (2003). The values of U_τ (or its equivalent, $C_f = 2(U_\tau/U_e)^2$) can also be compared with prior studies. For the smooth wall, the present value of $C_f = 0.0048$ ($Re_\theta = 870$) compares reasonably well with the following values obtained in a previous LDA study in an open channel flow (Tachie et al., 2003a): $C_f = 0.0053$ ($Re_\theta = 750$) and $C_f = 0.0048$ ($Re_\theta = 1020$). It should be noted that in the LDA study, sufficient data were obtained very close to the wall and the C_f values quoted above were determined from data in the viscous sublayer. For the upstream ribs, U_τ/U_e values for *d*-type, intermediate and *k*-type ribs (see Table 2) are only 4–7% different from the DNS results over transverse ribs (Leonardi et al., 2003). These differences are within the measurement uncertainty.

Fig. 10 shows semi-logarithmic plots of the mean velocity profiles over the smooth wall and ribs in inner coordinates. The smooth wall profile collapsed with the

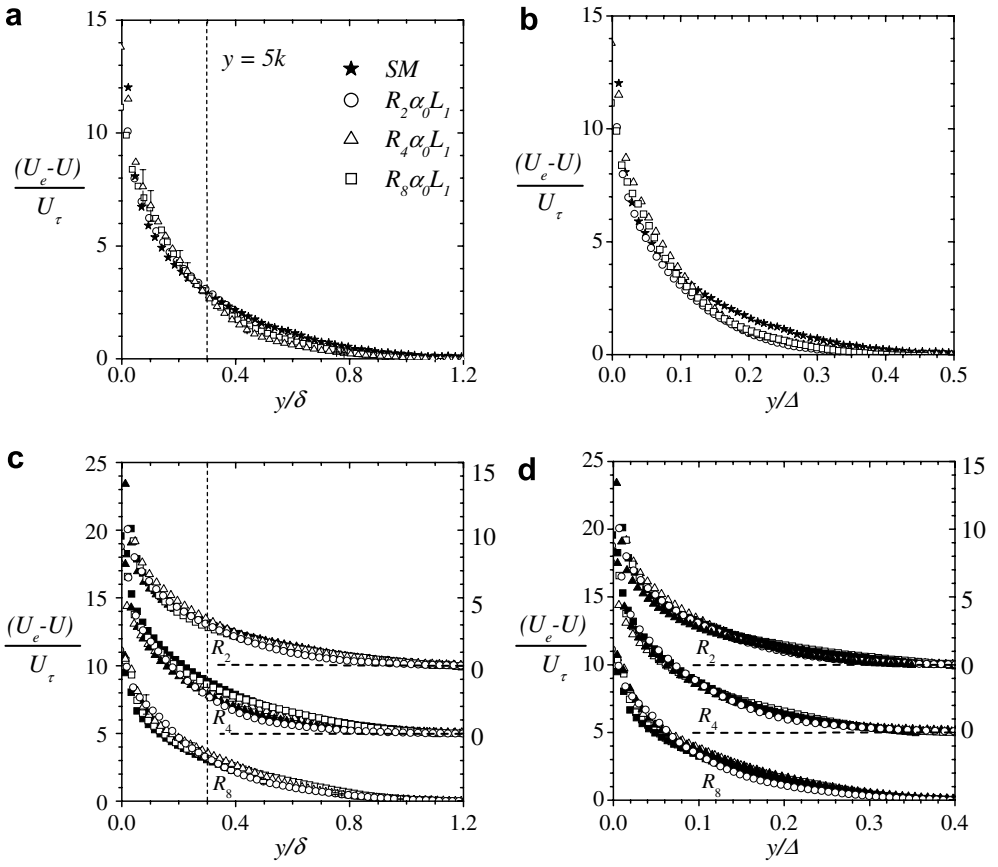

Fig. 11. Mean velocity defect profiles normalized by friction velocity. Note that in (a) and (c), y by δ; in (b) and (d), y by Δ. Vertical dotted lines in (a) and (c) correspond to the roughness sublayer.

log law over most of the boundary layer because of the negligible wake parameter ($\Pi \approx 0.02$). For the smooth and rib walls, values of Π were estimated from the relation: $\Delta U^+_{max} = 2\Pi/\kappa$, where ΔU^+_{max} is the maximum deviation of the experimental data in Fig. 10 from the log law, and should not be confused with the roughness function ΔB. Low to negligible values of the wake parameter have been reported in previous LDA measurements (Tachie et al., 2003b) carried out in open channel flows. Measurements obtained in ZPG turbulent boundary layer at elevated freestream turbulence levels (Hancock and Bradshaw, 1983; Thole and Bogard, 1996) show that Π decreases as the turbulence level increases. Thole and Bogard (1996) reported an asymptotic value of $\Pi = -0.5$. The wake parameter also varies with Reynolds number and is generally attenuated by favorable pressure gradient (FPG). The negligible wake component observed for the smooth wall profile may, therefore, be due to low Reynolds number effects, high background turbulence and the slight FPG. The profiles over the ribs show the expected downwards shift, ΔB. The amount of shift is smallest over the *d*-type ribs and largest over the *k*-type ribs. Fig. 10 and Table 2 demonstrate that values of Π over the ribs are clearly larger than the smooth wall value. A similar increase of Π values over various roughness elements was reported in ZPG (Krogstad and Antonia, 1999). The LDA study over a smooth wall, sand grains, wire mesh and perforated plate in an open channel (Tachie et al., 2000) and PIV measurements over three-dimensional hemispherical ribs in an open channel (Agelinchaab and Tachie, 2006) also showed higher Π values over the rough wall or ribs compared to the smooth wall value. In ZPG turbulent boundary layers, the higher Π values for rough walls have been attributed to higher wall shear stress and associated higher rate of boundary layer growth and entrainment of irrotational fluid into the boundary layer. It should be noted, however, that many other experiments over different types of roughness elements in ZPG turbulent boundary layer (Connelly et al., 2006) concluded that Π is independent of the specific surface condition.

The profiles obtained over the various rib types upstream of and within the converging section are shown in Figs. 10b, c and d. These figures and Table 2 can be used to study the effects of flow acceleration or FPG on the roughness function and wake parameter. It can be observed that as the flow accelerates over the ribs, the wake parameter is reduced. This implies that FPG tends to reduce the wake component and constrain the effects of rib roughness to the inner layer of the mean velocity profile. The differences observed in the roughness function are within measurement uncertainty.

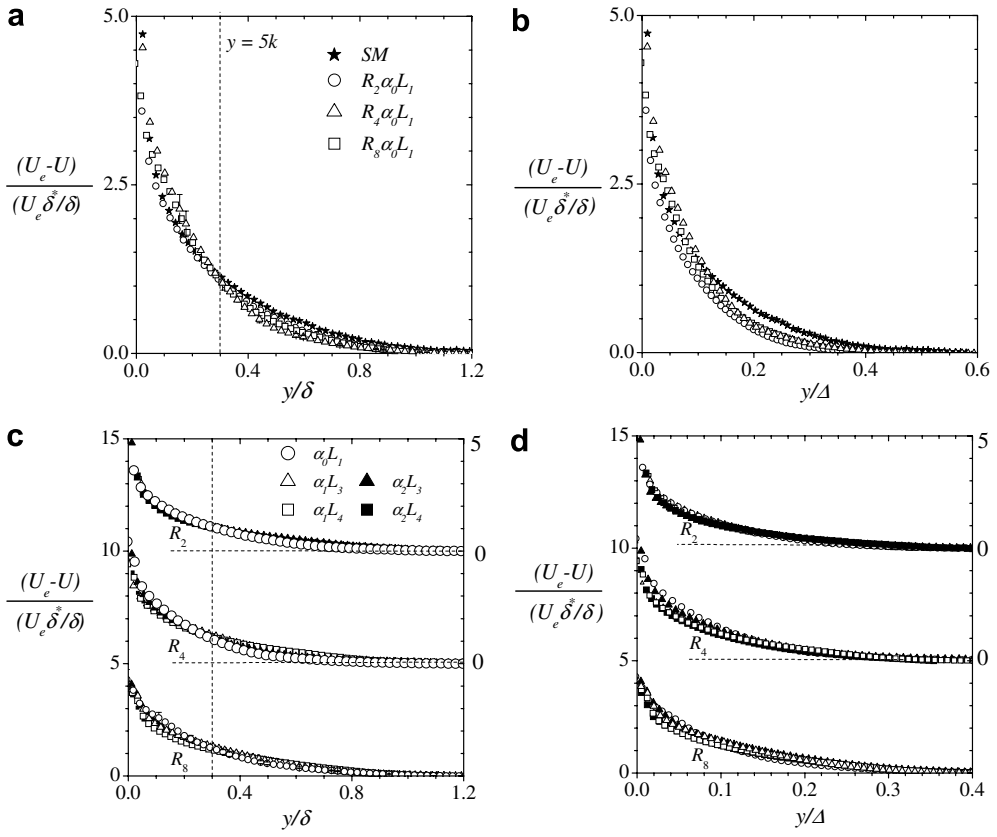

Fig. 12. Mean velocity defect profiles normalized by mixed scaling proposed by Zagarola and Smits (1998). Note that in (a) and (c), y by δ; in (b) and (d), y by Δ. Vertical dotted lines in (a) and (c) correspond to the roughness sublayer.

4.2.4. Drag characteristics

The values of U_τ/U_e, ΔB, k_s^+, k_s/k, k_s/δ and δ/Δ are summarized in Table 2. The equivalent sand grain Reynolds number, k_s^+, was determined from Eq. (2). Using the criteria proposed by Schlichting (1979), the *d*-type ribs are in transitionally rough regime while the intermediate and *k*-type ribs are in fully rough regime. It is observed that U_τ increases as the flow accelerates through the converging section. The rate of increase is approximately the same as in U_e so that U_τ/U_e remains approximately constant for a given rib type. The roughness functions ΔB and U_τ/U_e show that the drag characteristics increase with pitch ratio. The values of U_τ/U_e for the *k*-type ribs are nearly twice as large as the smooth wall value but those for the *d*-type ribs are only marginally higher than the smooth wall value. Leonardi et al. (2003) compiled values of ΔB obtained in their DNS work and several experiments. The value of $\Delta B \approx 2$ obtained in the present study for $p/k = 2$ is comparable to $2 < \Delta B < 4$ in the previous studies. Similarly, $\Delta B \approx 9$ obtained in the present study for $p/k = 4$ is consistent with $9 < \Delta B < 11$ in the previous studies while $\Delta B \approx 12$ in the present and previous studies.

The ratio k_s/k also varies significantly with rib type. For a given rib type, however, the variation of k_s/k with slope and axial location is not significant. The average value for the *d*-type rib is $k_s/k = 0.23$. This value is in good agreement with 0.27 obtained in PIV study over three-dimensional hemispherical spheres in an open channel (Agelinchaab and Tachie, 2006) but higher than 0.1 obtained in LES in fully developed channel. For the intermediate ribs, $k_s/k \approx 2.4$ in the present study compared with 3.2 in the LES study and 1.75 in the PIV experiments. Over the *k*-type ribs, the present value of $k_s/k \approx 7$ is higher than a value of 5.9 reported in LES and 4.16 in the PIV experiments. The k_s/k values also provide insight into the effectiveness of transverse square ribs to augment flow resistance compared to mono-disperse sand grains. For example, 21 mm diameter of mono-disperse sand grains covering the entire bottom wall of the channel will be required to produce the same flow resistance observed for the present *k*-type rib while only 0.6 mm diameter sand grains are necessary to produce the resistance observed over the *d*-type ribs. The above results show that although ribs of the same physical dimension were used in all the present experiments, the drag characteristics increase significantly as the rib spacing is increased. Therefore, the rib height *k* may not be a useful characteristic roughness length scale. If instead the equivalent sand grain height k_s is used as the characteristic roughness length scale, then, as shown in Table 2, this characteristic length scale is only

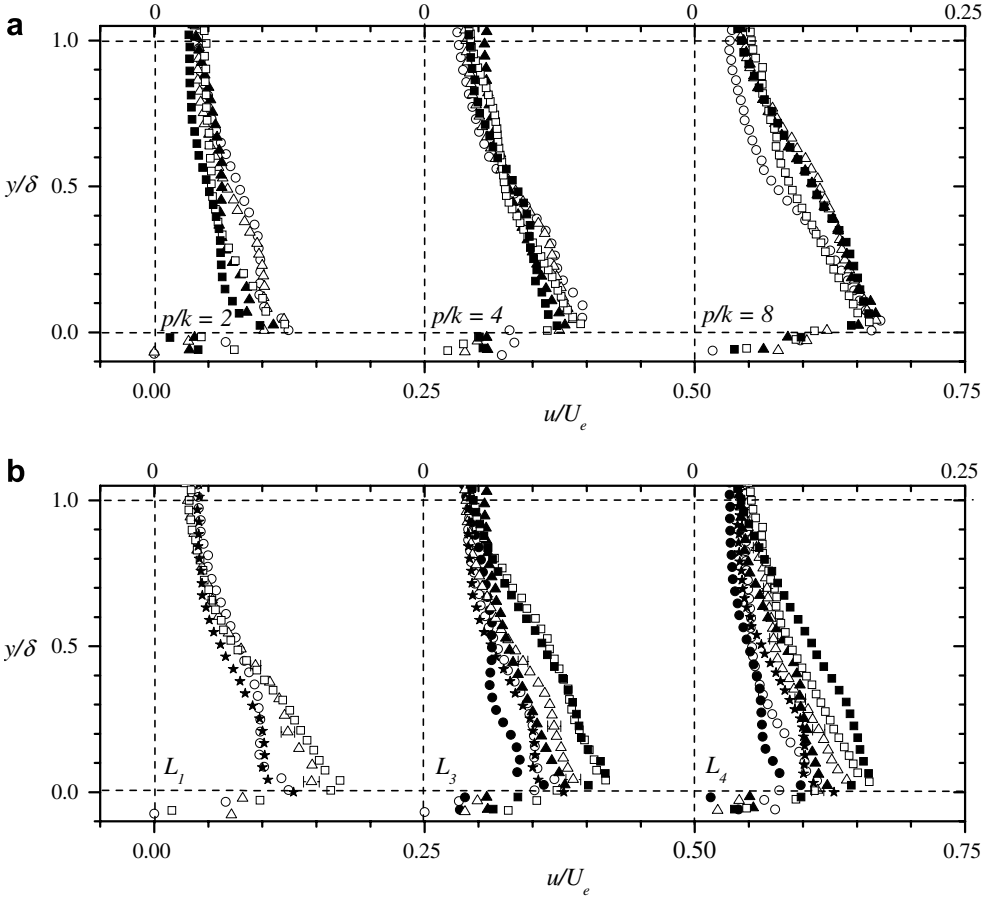

Fig. 13. Profiles of the spatial averaged streamwise turbulent intensity over the ribs in outer coordinates. Symbols are as in Fig. 9.

0.8–1.6% of the boundary layer thickness for d-type, 15% for intermediate and 40% for k-type. Similarly, the extent of the roughness sublayer ($y < 5k_s$) is up to 7% of the boundary layer over d-type ribs, 75% for intermediate and outside the boundary layer for the k-type ribs. The above analysis for k-type ribs is not physically sound. For the d-type ribs, however, we may conclude that k_s values are so small compared to the boundary layer thickness that the d-type ribs hardly modify the mean velocity profile. This may explain the observation that the mean velocity profile over the d-type ribs in the converging section show many of characteristics observed in accelerating flow over a smooth wall. For intermediate and k-type ribs, however, k_s values are a significant fraction of the boundary layer thickness. Under these conditions, the ribs modify the mean flow dramatically in the inner region. Table 2 demonstrates that δ/Δ is nearly independent of rib type, slope and axial location. The average value for all the 16 values reported in the table is $\delta/\Delta = 0.353 \pm 0.033$. The 10% variation from the mean velocity is comparable to measurement uncertainty in Δ. As noted earlier, Bergstrom et al. (2005) demonstrated that δ/Δ is invariant for ZPG turbulent boundary layers. However, their value of $\delta/\Delta = 0.255 \pm 0.02$ for smooth and rough wall ZPG experiments is lower than the present value.

4.2.5. Mean velocity defect profiles

The mean defect profiles obtained over the smooth wall and the upstream ribs are plotted in Figs. 11a and b while profiles obtained over a particular rib type are plotted together in Figs. 11c and d. The friction velocity U_τ is used to normalize all the profiles in Fig. 11. In Figs. 11a and c, the values of y are normalized by δ while Δ is used to normalize y in Figs. 11b and d. Figs. 11a and b can be used to study the effects of rib type on the mean velocity profile. The vertical dotted lines correspond to the roughness sublayer ($y = 5k$). The profiles over the intermediate and k-type ribs fall more rapidly compared to the smooth wall and d-type profiles. This is consistent with the larger Π values observed for the intermediate and k-type ribs. Outside the roughness sublayer, the rib profiles fall consistently below the smooth wall profile. The defect thickness Δ (Fig. 11b) collapses the profiles over the upstream ribs better, and tends to enhance the deviation of the rib profiles from the smooth profile. Figs. 11c and d may be used to study the effects of flow acceleration on a particular rib type. Fig. 11c reveals that for a particular rib type, the upstream profile falls more rapidly than those obtained within the converging section. This is a clear indication that FPG reduces the wake component irrespective of the specific surface condition. Fig. 11c also shows that, with

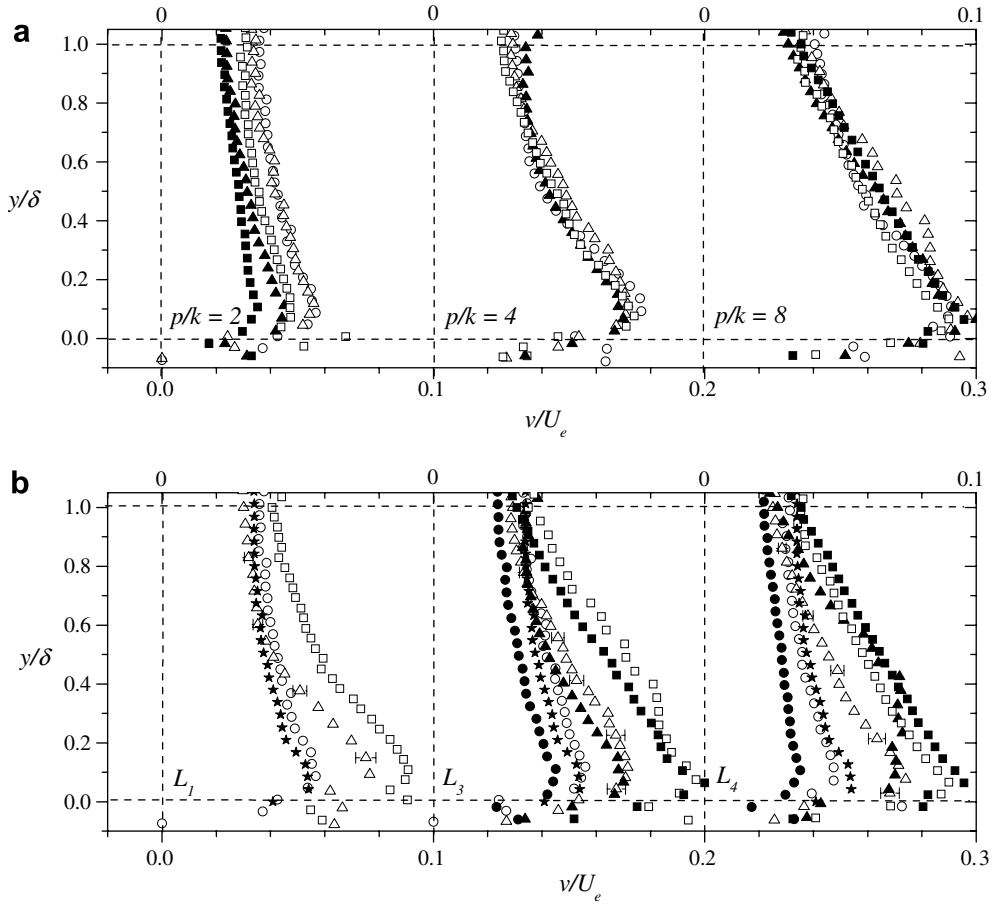

Fig. 14. Profiles of the spatial averaged transverse turbulent intensity over the ribs in outer coordinates. Symbols are as in Fig. 9.

exception of intermediate profiles, the upstream and downstream rib profiles collapse reasonably well when δ is used as the characteristic length scale. It appears that Δ does a better job in collapsing all the profiles (including those over the intermediate ribs) across most of the boundary layer (Fig. 11d). The defect profiles are re-plotted in Fig. 12 using the mixed scaling, $U_e\delta^*/\delta$, proposed by Zagarola and Smits (1998). This scaling does not produce any significant improvement in collapsing the profiles over the smooth wall and upstream ribs (Figs. 12a and b). However, over a particular rib type, the upstream profile and those obtained in the converging section are now nearly indistinguishable irrespective of the characteristic length scale used (Figs. 12c and d).

4.2.6. Turbulent intensities and Reynolds shear stress

The profiles of the streamwise and transverse turbulent intensities, normalized by U_e and δ, are shown in Figs. 13 and 14. In Figs. 13a and 14a, profiles obtained over a particular rib type but at various axial locations and slopes are plotted together. Figs. 13b and 14b show profiles obtained at a particular axial location but over different rib types. Fig. 13a shows that the peak values of the streamwise turbulent intensity do not vary significantly with slope or location. However, as the flow accelerates through the converging sections, the profiles over d-type ribs fall rapidly from their peak value. As a result, the turbulent intensity in the region $y/\delta < 0.5$ decreases dramatically with increasing flow acceleration. Over the intermediate ribs, an increase in flow acceleration results in a modest decrease in turbulence intensity close to the ribs. No systematic effects of flow acceleration are observed close the k-type profiles. At L_1, the smooth wall and d-type profiles collapse reasonably well across the boundary layer. Inside the converging sections, the absolute values of u over the d-type ribs do not change significantly. However, the increase in U_e values in the converging sections causes the dimensionless u-profiles over the d-type ribs at L_3 and L_4 to drop significantly below the smooth wall profile. The intermediate and k-type ribs enhance the turbulence level substantially over most of the boundary layer. For example, $(u/U_e)_{\max}$ values obtained over the intermediate and k-type ribs are 30–40% and 50–65%, respectively, higher than the smooth wall value. Similarly, the level of transverse turbulence intensity, v/U_e, over the d-type ribs decreases as flow acceleration increases through the converging section. There is no significant variation of v/U_e with axial location and

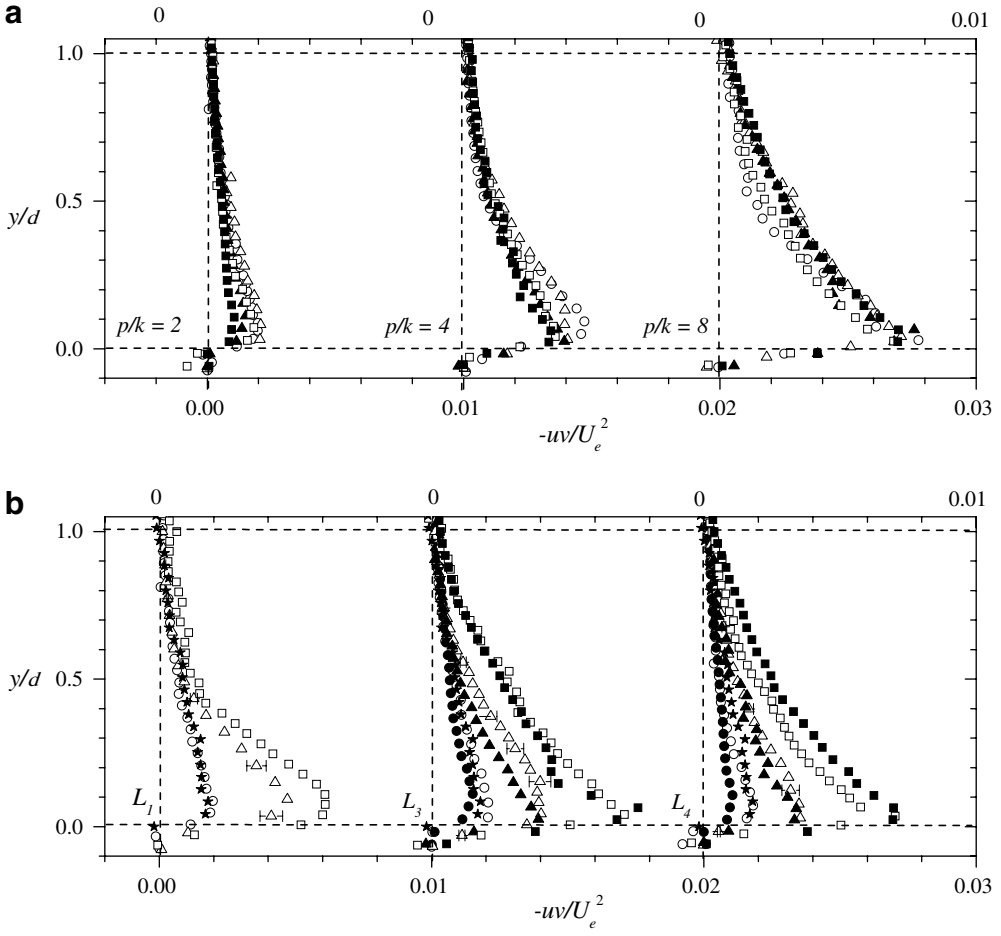

Fig. 15. Profiles of the spatial averaged Reynolds shear stress over the ribs in outer coordinates. Symbols are as in Fig. 9.

slope over the intermediate and k-type ribs. Compared to the smooth wall, v profiles obtained over intermediate and k-type profiles are substantially higher over most of the boundary layer while those over d-type in the converging section decreased. At the last measurement station (L_4), for example, values of $(v/U_e)_{\max}$ over the intermediate and k-type ribs are, respectively, 35% and 75% higher than the smooth wall value. On the other hand, the value of $(v/U_e)_{\max}$ for the d-type rib at L_4 in the $\alpha = 2°$ test section is 30% lower than the smooth value.

The variation of the Reynolds shear stress profiles over the upstream ribs and those within the converging section is qualitatively similar to the turbulence intensities. In fact, the effects of rib type are even more pronounced here than observed for the turbulent intensities. At L_1, the value of $(-uv/U_e^2)_{\max}$ over the d-type ribs is identical to the smooth wall value but those over the intermediate and k-type ribs are, respectively, about 130% and 200% higher than the smooth wall value. Results obtained from previous LES and measurements in both fully developed channel and

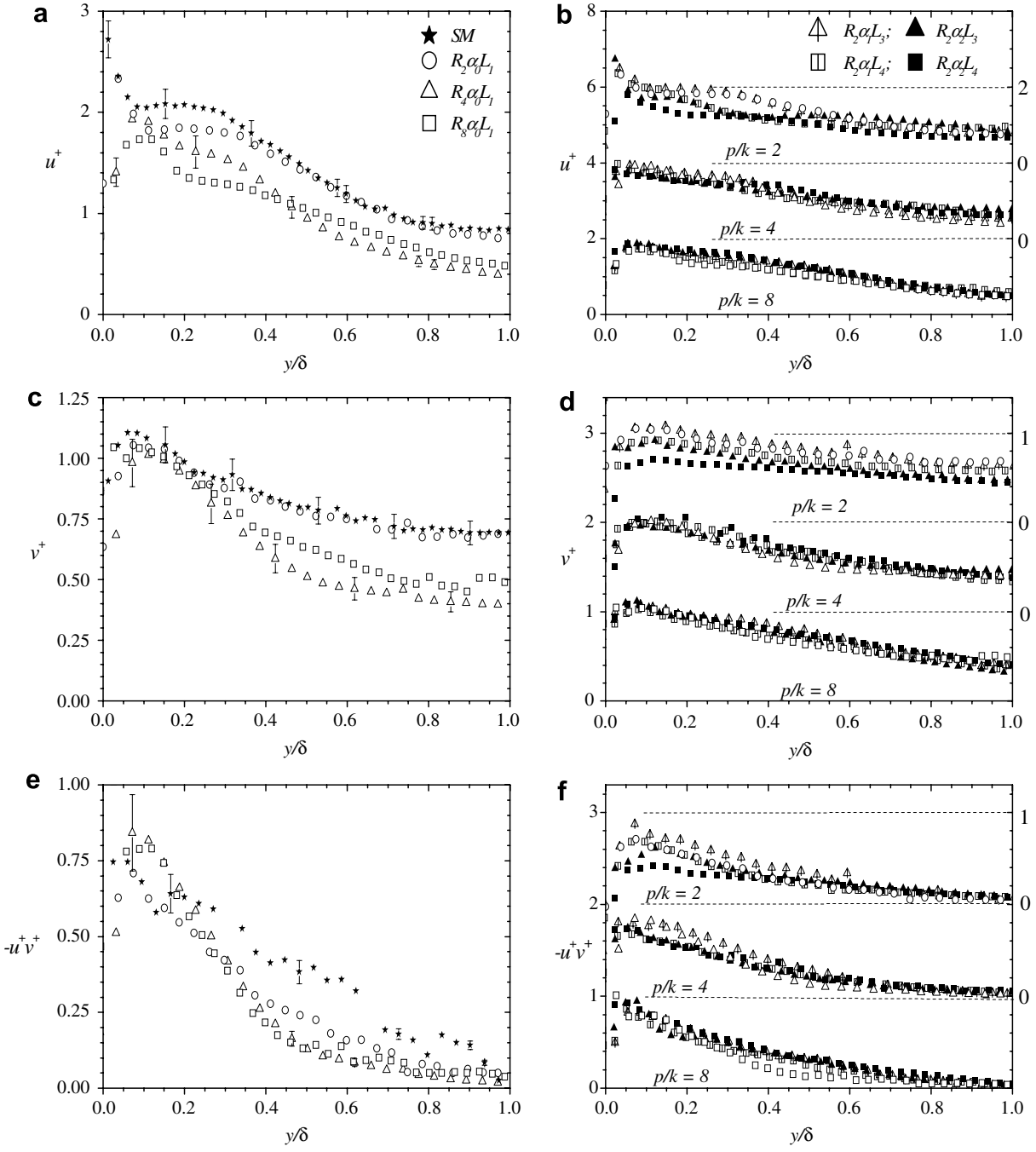

Fig. 16. Profiles of turbulent intensities and Reynolds shear stress normalized by friction velocity. Symbols in (c) and (e) are as in (a); symbols in (d) and (f) are as in (b).

ZPG show that the turbulent intensities and Reynolds shear stress increase with increasing pitch ratio. The reduction in the peak values of $-uv$ over the *d*-type ribs in the converging sections is quite dramatic. For a two-dimensional incompressible flow, positive $\partial U/\partial x$ (FPG) is associated with negative $\partial V/\partial y$. It has been suggested that negative $\partial V/\partial y$ tends to flatten the large eddies and reduce their contribution to the Reynolds stress (Townsend, 1961). This implies that FPG should decrease the Reynolds stresses. This explanation is valid for the *d*-type ribs but not for the *k*-type ribs. Another important observation from Fig. 15 is that the Reynolds shear stress profiles fall more rapidly from their peak values than the near-linear variation reported in fully developed channels. This may be explained by noting that for non-zero pressure gradient turbulent flows, the variation of the Reynolds shear stress in the inner region can be approximated as $-uv = \tau_w + (\mathrm{d}P_e/\mathrm{d}x)y$. This relation shows that, for pressure gradient turbulent flows, the change in slope of the Reynolds shear stress could be substantial in the wall region. Indeed, for a FPG (negative $\mathrm{d}P_e/\mathrm{d}x$) values of $-uv$ should be lower than if $\mathrm{d}P_e/\mathrm{d}x \approx 0$.

The turbulent intensities and Reynolds shear stress, normalized by the friction velocity, are shown in Fig. 16. Close to the ribs, the values of u^+ over the upstream ribs (Fig. 16a) are distinctly lower than the smooth wall values. In the near-wall region, the u^+ profiles also become more blunt as the pitch ratio increases. Krogstad et al. (2005)

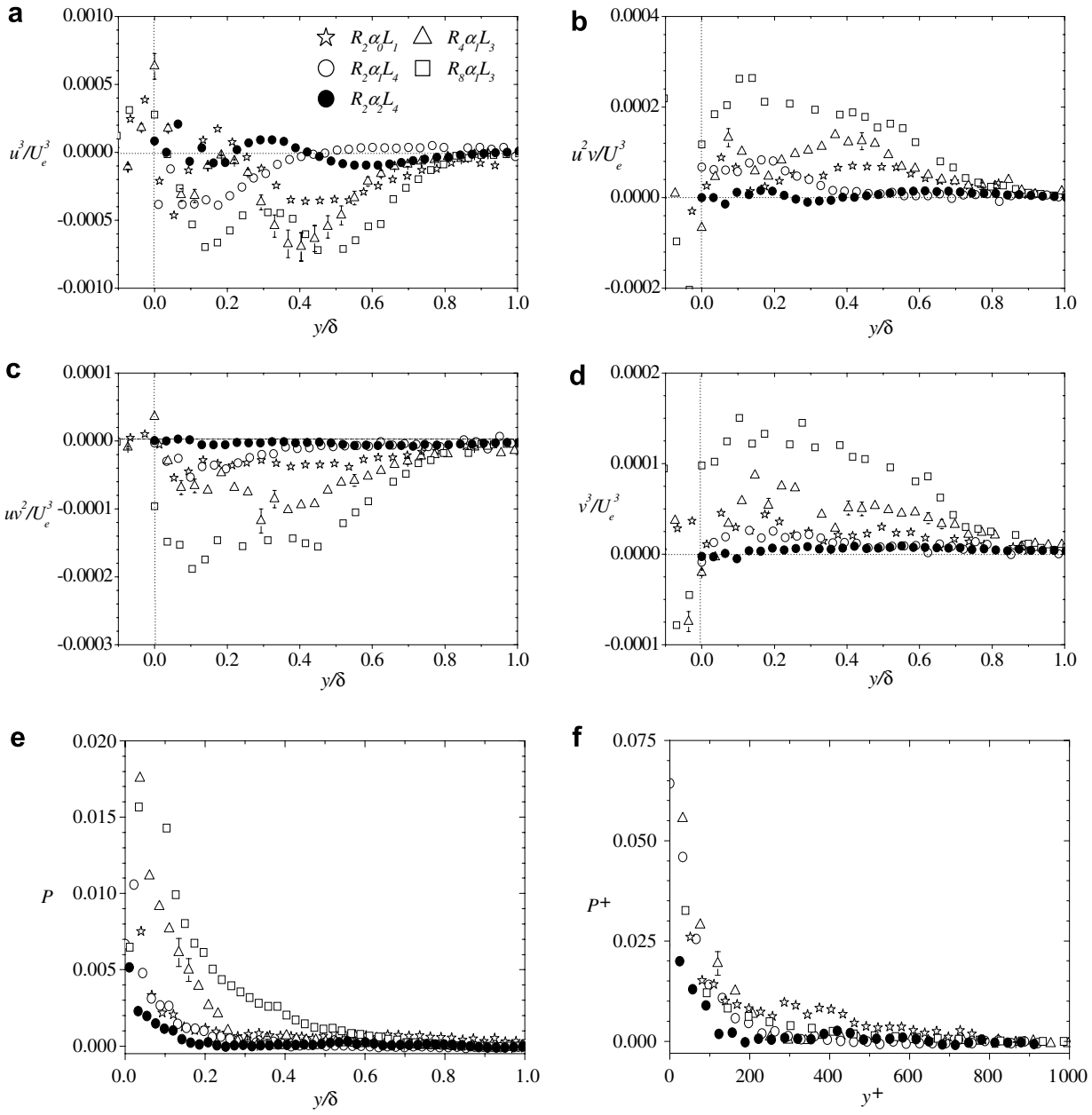

Fig. 17. Profiles of triple products and turbulence production: (a) u^3, (b) u^2v, (c) uv^2 (d) v^3; (e) and (f) are production in outer and inner variables.

suggested that significant reduction in u^+ close to rough walls is due to break-up of the streamwise vortices by the roughness elements. Further, for a smooth wall, the peak and near-wall spike in u^+ are due to viscous effects. The u^+ profiles close to the d-type ribs are peaky since the d-type is in transitionally rough regime and viscous drag constitutes a significant fraction of the total drag. The near-wall spike in u^+ are, however, absent over the intermediate and k-type ribs because flow over these ribs are in fully rough regime and viscous effects are negligible. Upstream of the converging section, the near-wall values of v^+ and $-u^+v^+$ (Figs. 16c and e) are nearly independent of rib type. Since U_τ/U_e does not vary significantly along the channel over a particular ribs, the variation of the turbulence intensities (Figs. 16b and d) and Reynolds shear stress (Fig. 16f) over a particular rib type is essentially the same as observed in Figs. 13–15. That is, flow acceleration has no significant effects on the turbulent intensities and Reynolds shear stress profiles over intermediate and k-type ribs. For the d-type ribs, on the other hand, flow acceleration reduces the turbulent intensities and Reynolds shear stress in the region $y/\delta < 0.4$.

4.3. Triple products and turbulence production

In this section, five selected test cases are used to discuss the effects of flow acceleration and rib roughness on triple products and turbulence production. Because profiles over d-type ribs are most sensitive to flow acceleration while those over the intermediate and k-type ribs are not, the five test conditions were selected to comprise the d-type ribs with the least, intermediate and highest flow acceleration ($R_2\alpha_0L_1$, $R_2\alpha_1L_4$ and $R_2\alpha_2L_4$), intermediate ribs ($R_4\alpha_1L_3$) and k-type ribs ($R_8\alpha_1L_3$). The profiles of u^3, u^2v, uv^2 and v^3 are shown in Figs. 17a–d. These profiles can provide some insight into turbulent diffusion terms in the transport equations for the turbulent kinetic energy and Reynolds stresses. The quantity u^3, for example, represents the transport of u^2 by turbulent motion in the streamwise direction; u^2v and v^3 correspond, respectively, to the transport of u^2 and v^2 in the transverse direction while uv^2 is associated with 'turbulent work' done by the Reynolds stress. Figs. 17a and c show that u^3 and uv^2 are predominantly negative across the boundary layer while u^2v and v^3 (Figs. 17b and d) are positive. The triple products are highest for k-type and least for d-type ribs, and these differences are observed across most of the boundary layer. Flow acceleration reduces the magnitude of the triple products over the d-type ribs dramatically. Note that for $R_2\alpha_2L_4$, turbulence is significantly reduced and the quantities u^2v, uv^2 and v^3 are nearly zero across the entire boundary layer. In some case (e.g., u^3 and u^2v), the trend of the d-type profiles also varies substantially with flow acceleration. The levels of u^3 are significantly higher than the other triple products. However, it is the gradients of these quantities that are most relevant to turbulent transport. Most of the Reynolds shear stress is produced immediately above the top plane of the ribs and then diffused ($\partial uv^2/\partial y$) outwards into the outer layer and wall wards into the cavities. Similarly, the peak values of u^2v and v^3 occur above the top plane of the ribs. Since $-\partial(u^2v + v^3)/\partial y$ is associated with diffusion of turbulent kinetic energy in the transverse direction, Figs. 17b and d imply that turbulent kinetic energy is diffused outwards into the outer layer and wall wards into the cavities.

The full transport equations for the Reynolds stresses and turbulent kinetic energy can be found in Hinze (1959). For a two-dimensional turbulent flow, the production terms in u^2 and v^2 are, respectively, $P_{uu} = -u^2\partial U/\partial x - uv\partial U/\partial y$ and $P_{vv} = -v^2\partial V/\partial y - uv\partial V/\partial x$. Similarly, the production term in the turbulent kinetic energy equation is $P_k = [-uv(\partial U/\partial y + \partial V/\partial x)] - [u^2\partial U/\partial x + v^2\partial V/\partial y]$. Figs. 17e and f show the total production of the turbulent kinetic energy (P_k). The production by the normal stresses $[u^2\partial U/\partial x + v^2\partial V/\partial y]$ was also evaluated. Although this term is non-zero, its contribution to P_k is small over most of the boundary layer. It was also found that $\partial U/\partial y \gg \partial V/\partial x$ so that $-uv\partial U/\partial y$ is the most dominant production term. This implies that the production terms in the transport equation for the streamwise Reynolds stress and turbulent kinetic energy are nearly the same (i.e., $P_k \approx P_{uu}$). Fig. 17e implies that the level of turbulence production increases with pitch ratio which is consistent with the observation that values of $-uv$ increase with pitch ratio. The region of non-negligible production is limited to the immediate vicinity of the d-type ribs ($y/\delta < 0.2$) because variation of U with y is significant only close to the ribs. Because of the relatively higher drag characteristics of the intermediate and k-type ribs, the local velocity is reduced below the freestream value over most of the boundary layer. This produces non-negligible values of $\partial U/\partial y$ (and therefore turbulence production) across most of the boundary layer. The high levels of the streamwise turbulent intensity observed over the intermediate and k-type ribs are consistent with the high production term over these ribs. The higher transverse turbulent intensities over the intermediate and k-type ribs cannot be explained by the production term, $(-v^2\partial V/\partial y - uv\partial V/\partial x)$. It is likely that energy is removed from the streamwise stresses and redistributed to the transverse stresses. When normalized with wall variables (Fig. 17f), the production term becomes nearly universal in the outer region.

5. Conclusions

The present results provide additional evidence that, in the absence of favorable pressure gradient, rib roughness enhances the drag characteristics and the wake parameter compared to smooth wall values. Compared to a smooth wall, rib roughness is more effective in increasing mass flux deficit than in augmenting momentum flux deficit. Interaction between the overlying boundary layer and d-type cavities is negligible and so flow over d-type ribs is largely undisturbed. The implications of this for the mean flow

are that the equivalent sand grain roughness height is only 1.5% of the boundary layer thickness, and the drag coefficient is similar or only marginally higher than the smooth wall value. The profiles of turbulent intensities and Reynolds shear stress over the upstream *d*-type are either identical or only marginally higher than the corresponding smooth wall profile. On the other hand, very strong interaction occurred between the *k*-type cavities and the overlying boundary layer. In this case, the mean momentum flux along the interface is high, exceeding the Reynolds shear stress at some locations. The stronger interaction between the shear layers produces significantly higher turbulent levels over *k*-type ribs than *d*-type ribs. The turbulent intensities, Reynolds shear stress and turbulence production also increase with pitch ratio.

Favorable pressure gradient or flow acceleration has no significant effects on drag characteristics but tends to reduce the effectiveness of rib roughness to augment mass flux deficit in comparison to momentum flux deficit. Flow acceleration reduces the wake parameter irrespective of rib type. The mixed scaling proposed by Zagarola and Smits (1998) collapsed the mean defect profiles over the ribs extremely well across the boundary layer. Flow acceleration does not have any significant effects on the turbulent quantities over the intermediate and *k*-type ribs. Since these two rib surfaces are in the fully rough regime and their drag characteristics are significantly higher than the smooth wall value, the inner regions of the intermediate and *k*-type ribs are largely adamant to the well documented effects of FPG on smooth wall turbulent flow. The flow over the *d*-type ribs, on the other hand, bears many of the hallmarks of accelerating flow over a smooth wall. For example, their mean velocity profiles become 'more full' and eventually collapsed onto the smooth wall profile. Turbulent intensities and Reynolds shear stress over the *d*-type ribs decrease dramatically with flow acceleration and eventually fall significantly below the upstream smooth wall profiles. Triple products and turbulence production over the *d*-type ribs are also attenuated by flow acceleration.

Acknowledgments

The financial support provided by Canada Foundation for Innovation, Natural Sciences and Engineering Research Council of Canada and Manitoba Hydro is gratefully acknowledged.

References

Agelinchaab, M., Tachie, M.F., 2006. Open channel turbulent flow over hemispherical ribs. Int. J. Heat Fluid Flow, in press, doi:10.1016/j.ijheatfluidflow.2006.03.001.

Ashrafian, A., Anderson, H.I., Manhart, M., 2004. DNS of turbulent flow in a rod-roughened channel. Int. J. Heat Fluid Flow 27, 65–79.

Bakken, O.M., Krogstad, P.-Å., Ashrafian, A., Andersson, H.I., 2005. Reynolds number effects in the outer layer of the turbulent flow in a channel with rough walls. Phys. Fluids 17, 1–16.

Bandyopadhyay, P.R., 1987. Rough-wall turbulent boundary layers in the transition regime. J. Fluid Mech. 180, 231–266.

Bergstrom, D.J., Akinlade, O.G., Tachie, M.F., 2005. Skin friction correlation for smooth and rough wall turbulent boundary layers. J. Fluids Eng. 127, 1146–1153.

Blackwelder, R.F., Kovasznay, L.S.G., 1972. Large-scale motion of a turbulent boundary layer during relaminarization. J. Fluid Mech. 53, 61–83.

Clauser, F.H., 1954. Turbulent boundary layers in adverse pressure gradient. J. Aero. Sci. 21, 91–108.

Coleman, H.W., Steele, W.G., 1995. Engineering application of experimental uncertainty analysis. AIAA J. 33, 1888–1896.

Connelly, J.S., Schultz, M.P., Flack, K.A., 2006. Velocity-defect scaling for turbulent boundary layers with a range of relative roughness. Exp. Fluids 40, 188–195.

Cui, J., Patel, V.C., Lin, C.-L., 2003. Large-eddy simulation of turbulent flow in a channel with rib roughness. Int. J. Heat Fluid Flow 24, 372–388.

Djenidi, R., Elavarasan, R., Antonia, R.A., 1999. The turbulent boundary layer over transverse square cavities. J. Fluid Mech. 395, 271–294.

Forliti, D.J., Strykowski, P.J., Debatin, K., 2000. Bias and precision of digital particle image velocimetry. Exp. Fluids 28, 436–447.

Furuya, Y., Fujita, H., 1967. Turbulent boundary layers on wire-screen roughnesses. Japan Soc. Mech. Eng. 10, 77–86.

Hama, F., 1954. Boundary layer characteristics for smooth and rough surfaces. Trans. Soc. Naval Architects Marine Engineers, USA 62, 333–351.

Hancock, P.E., Bradshaw, P., 1983. Effect of freestream turbulence on turbulent boundary layers. J. Fluid Eng. 105, 284–289.

Hinze, J.O., 1959. Turbulence: An Introduction to its Mechanism and Theory. McGraw-Hill, New York.

Jiménez, J., 2004. Turbulent flows over rough walls. Ann. Rev. Fluid Mech. 36, 173–196.

Johansson, A.V., Alfredsson, P.H., 1983. Effects of imperfect spatial resolution on measurements of wall-bounded turbulent shear flow. J. Fluid Mech. 137, 411–423.

Kameda, T., Mochizuki, S., Osaka, H., 2004. LDA measurement in roughness sub-layer beneath turbulent boundary layer developed over two-dimensional square rough surface. In: 12th International Symposium on Applications of Laser Techniques to Fluid Mechanics, Lisbon, Portugal 12–15 July.

Krogstad, P.Å., Antonia, R.A., 1999. Surface roughness effects in turbulent boundary layers. Exp. Fluids 27, 450–460.

Krogstad, P.-Å., Andersson, H.I., Bakken, O.M., Ashrafian, A., 2005. An experimental and numerical study of channel flow with rough walls. J. Fluid Mech. 530, 327–352.

Leonardi, S., Orlandi, P., Smalley, R.J., Djenidi, L., Antonia, R.A., 2003. Direct numerical simulations of turbulent channel flow with transverse square bars on one wall. J. Fluid Mech. 491, 229–238.

Leonardi, S., Orlandi, P., Antonia, R.A., 2005. A method for determining the frictional velocity in a turbulent channel floor with roughness on the bottom wall. Exp. Fluids 38, 796–800.

Ligrani, P.M., Moffat, R.J., 1986. Structure of transitionally rough and fully rough turbulent boundary layers. J. Fluid Mech. 162, 69–98.

Millikan, C.B., 1938. A critical discussion of turbulent flows in channels and circular tubes. In: Proceedings of 5th International Congress of Applied Mechanics, Cambridge.

Nikuradse, J., 1933. Strömungsgesetze in Rauhen Rohren, VDI-Forsch. 361 (Engl. Transl. 1950. Laws of flow in rough pipes. NACA TM 1292).

Perry, A.E., Schofield, W.H., Joubert, P.N., 1969. Rough wall turbulent boundary layers. J. Fluid Mech. 37, 383–413.

Piirto, M., Saarenrinne, P., Eloranta, H., Karvinen, R., 2003. Measuring turbulence energy with PIV in backward-facing step flow. Exp. Fluids 35, 219–236.

Prasad, A.K., Adrian, R.J., Landreth, C.C., Offutt, P.W., 1992. Effect of resolution on the speed and accuracy of particle image velocimetry interrogation. Exp. Fluids 13, 105–116.

Saikrishnan, N., Marusi, I., Longmire, E.K., 2006. Assessment of dual plane PIV measurements in wall turbulence using DNS data. Exp. Fluids 41, 265–278.

Schlichting, H., 1979. Boundary-layer Theory. McGraw-Hill, New York.

Smalley, R.J., Antonia, R.A., Djenidi, L., 2001. Self-preservation of rough-wall turbulent boundary layers. Eur. J. Mech. B 20, 591–602.

Tachie, M.F., Bergstrom, D.J., Balachandar, R., 2000. Rough wall turbulent boundary layers in shallow open channel flow. J. Fluid Eng. 122, 533–541.

Tachie, M.F., Bergstrom, D.J., Balachandar, R., 2003a. Roughness effects in low-Re_θ open channel turbulent boundary layers. Exp. Fluids 35, 338–346.

Tachie, M.F., Bergstrom, D.J., Balachandar, R., 2003b. Low Reynolds number effects in open channel flows. Exp. Fluids 34, 616–624.

Tani, I., 1987. Equilibrium, or nonequilibrium, of turbulent boundary layer flows. Proc. Jpn. Acad. B 63, 96–100.

Thole, K.A., Bogard, D.G., 1996. High freestream turbulence effects on turbulent boundary layers. J. Fluids Eng. 118, 276–284.

Townsend, A.A., 1961. Equilibrium layers and wall turbulence. J. Fluid Mech. 11, 97–120.

Zagarola, M.V., Smits, A.J., 1998. Mean-flow scaling of turbulent pipe flow. J. Fluid Mech. 373, 33–79.